ATLAS NOTE
ATLAS-CONF-2016-026
May 22, 2016

Measurements of long-range azimuthal anisotropies and associated Fourier coefficients in pp collisions at $\sqrt{s}$ = 5.02 and 13 TeV and p+Pb collisions at $\sqrt{s_{\mathrm{NN}}}$ = 5.02 TeV with the ATLAS detector

The ATLAS Collaboration

Abstract

Results are presented from ATLAS measurements of two-particle correlations in $\sqrt{s}$ = 5.02 and 13 TeV pp collisions and in $\sqrt{s_{\mathrm{NN}}}$ = 5.02 TeV p+Pb collisions at the LHC. The correlation functions are measured as a function of relative azimuthal angle, $\Delta\phi$, and pseudorapidity, $\Delta\eta$, using charged particles detected within the pseudorapidity interval $|\eta|<2.5$. Azimuthal modulation in the long-range component of the correlation function, with $|\Delta\eta|>2$, is studied using a template fitting procedure to remove a "back-to-back" contribution to the correlation function that primarily arises from hard-scattering processes. In addition to the elliptic, $\cos(2\Delta\phi)$, modulation observed in a previous measurement, the pp correlation functions exhibit significant $\cos(3\Delta\phi)$ and $\cos(4\Delta\phi)$ modulation. The Fourier coefficients, $v_{n,n}$, associated with the $\cos(n\Delta\phi)$ modulation of the correlation functions for n = 2–4 are measured as a function of charged-particle multiplicity, $N_{\mathrm{ch}}^{\mathrm{rec}}$, and charged particle transverse momentum, p_{T}. The Fourier coefficients are observed to be compatible with $\cos(n\phi)$ modulation of per-event single-particle azimuthal angle distributions. The single particle Fourier coefficients, v_n, are measured as a function of charged particle multiplicity, $N_{\mathrm{ch}}^{\mathrm{rec}}$, and charged particle transverse momentum, p_{T} for n= 2–4.

ATLAS-CONF-2016-026
02 June 2016

1 Introduction

Observations of azimuthal anisotropies in the angular distributions of particles produced in proton–lead (p+Pb) collisions at the LHC [1–5] and in deuteron–gold (d+Au) [6–8] and ^{3}He + Au [9] collisions at RHIC have garnered much interest due to the remarkable similarities between the phenomena observed in those colliding systems and the effects of collective expansion seen in the Pb+Pb and Au+Au collisions [3, 10–13]. [1] The most intriguing feature of the azimuthal anisotropies is the "ridge" – an enhancement in the production of particles with small azimuthal-angle (ϕ) separation that extends over a large range of pseudorapidity (η) separation [1, 2, 14, 15]. In Pb+Pb [3, 10–13] and p+Pb [1–3] collisions, the ridge is understood to result from sinusoidal modulation of the single-particle azimuthal angle distributions, and the characteristics of the modulation, for example the p_{T} dependence [16], are remarkably similar in the two systems [4].

While the modulation of the azimuthal angle distributions in Pb+Pb collisions is understood to result from geometry of the initial state and the imprinting of that geometry on the angular distributions of the particles by the collective expansion (see e.g. [17–19] and references therein), there is, as yet, no consensus that the modulation observed in p+Pb collisions results from the same mechanism. Indeed, an alternative explanation for the modulation using perturbative QCD and assuming saturated parton distributions in the lead nucleus is capable of reproducing many features of the p+Pb data [20–29]. Nonetheless, because of the many similarities between the p+Pb and Pb+Pb observations, extensive theoretical and experimental effort has been devoted to addressing the question of whether the strong-coupling physics understood to be responsible for the collective dynamics in A+A collisions may persist in smaller systems [30–40].

A recent study by the ATLAS Collaboration of two-particle angular correlations in proton–proton (pp) collisions at center-of-mass energies of $\sqrt{s}$ = 13 and 2.76 TeV obtained results consistent with the presence of an elliptic or $\cos(2\phi)$ modulation of the per-event single particle azimuthal angle distributions [41]. This result suggests that the ridge previously observed in $\sqrt{s}$ = 7 TeV pp collisions [14] results from modulation of the single-particle azimuthal angle distributions similar to that seen in Pb+Pb and p+Pb collisions. Indeed, the p_{T} dependence of the modulation was similar to that observed in the other systems. Surprisingly, the amplitude of the modulation relative to the average differential particle yield, $\langle \mathrm{d}n/\mathrm{d}\phi \rangle$, was observed to be constant, within uncertainties, as a function of the charged particle multiplicity of the pp events and to be consistent between the two energies, suggesting that the modulation is an intrinsic feature of high-energy pp collisions. These results provide further urgency to address the question of whether strong-coupling and collective dynamics play a significant role in small systems including the smallest systems accessible at collider energies – pp collisions. Since the elliptic modulation observed in the pp data is qualitatively similar to that seen in p+Pb collisions, a direct, quantitative comparison of pp and p+Pb measurements is necessary for evaluating whether the phenomena are related.

The modulation of the single-particle azimuthal angle distributions in A+A, p/d+A, and, most recently, pp collisions is typically characterized using a set of Fourier coefficients, v_n, that describe the relative amplitudes of the sinusoidal components of the single-particle distributions. More explicitly, the azimuthal

[1] However, Ref. [8] argues that the observed correlations may be due to poorly understood hard-scattering contributions.

angle distributions of the particles are parameterized according to:

$$\frac{\mathrm{d}N}{\mathrm{d}\phi} = \left\langle \frac{\mathrm{d}N}{\mathrm{d}\phi} \right\rangle \left(1 + \sum_n 2v_n \cos\left[n\left(\phi - \Psi_n\right) \right] \right), \tag{1}$$

where the average in the equation indicates an average over azimuthal angle. Here, Ψ_n represents one of the n angles at which the nth-order harmonic is maximum; it is frequently referred to as the event plane angle for the nth harmonic. In Pb+Pb collisions, $n = 2$ modulation is understood to primarily result from an elliptic anisotropy of the initial state for collisions with non-zero impact parameter; that anisotropy is subsequently imprinted onto the angular distributions of the produced particles by the collective evolution of the medium producing an elliptic modulation of the produced particle azimuthal angle distributions in each event [17, 42, 43]. The higher ($n > 2$) harmonics are understood to result from position-dependent fluctuations in the initial-state energy density which produce higher-order spatial eccentricities that similarly get converted into sinusoidal modulation of the single-particle $\mathrm{d}N/\mathrm{d}\phi$ distribution by the collective dynamics [44–51]. Significant v_n values have been observed in Pb+Pb (p+Pb) collisions up to $n = 6$ [13] ($n = 5$ [4]). An important, outstanding question is whether $n > 2$ modulation is present in pp collisions.

The v_n coefficients can be measured using two-particle angular correlation functions, which, when evaluated as a function of $\Delta\phi \equiv \phi_b - \phi_a$, where a and b represent the two particles used to construct the correlation function, have an expansion similar to that in Eq. (1):

$$\frac{\mathrm{d}N}{\mathrm{d}\Delta\phi} = \left\langle \frac{\mathrm{d}N_{\mathrm{pair}}}{\mathrm{d}\Delta\phi} \right\rangle \left[1 + \sum_n 2v_{n,n} \cos\left(n\Delta\phi\right) \right]. \tag{2}$$

If the modulation of the two-particle correlation function arises solely from the modulation of the single-particle distributions, then, $v_{n,n} = v_n^2$. Often, the two-particle correlations are measured using different transverse momentum (p_{T}) ranges for particles a and b. Since the modulation is observed to vary with p_{T}, then

$$v_{n,n}(p_{\mathrm{T}}^{\mathrm{a}}, p_{\mathrm{T}}^{\mathrm{b}}) = v_n(p_{\mathrm{T}}^{\mathrm{a}}) v_n(p_{\mathrm{T}}^{\mathrm{b}}), \tag{3}$$

if the modulation of the correlation function results solely from single-particle modulation. [2] This "factorization" hypothesis can be tested experimentally by measuring $v_{n,n}(p_{\mathrm{T}}^{\mathrm{a}}, p_{\mathrm{T}}^{\mathrm{b}})$ for different ranges of $p_{\mathrm{T}}^{\mathrm{b}}$ and estimating $v_n(p_{\mathrm{T}}^{\mathrm{a}})$ using

$$v_n(p_{\mathrm{T}}^{\mathrm{a}}) = v_{n,n}(p_{\mathrm{T}}^{\mathrm{a}}, p_{\mathrm{T}}^{\mathrm{b}}) / \sqrt{v_{n,n}(p_{\mathrm{T}}^{\mathrm{b}}, p_{\mathrm{T}}^{\mathrm{b}})}. \tag{4}$$

and evaluating whether $v_n(p_{\mathrm{T}}^{\mathrm{a}})$ depends on the choice of $p_{\mathrm{T}}^{\mathrm{b}}$.

In addition to the sinusoidal modulation, the two-particle correlation functions include contributions from hard-scattering processes that produce a jet peak centered at $\Delta\phi = \Delta\eta = 0$ and a dijet enhancement at $\Delta\phi = \pi$ that extends over a wide range of $\Delta\eta$. The jet peak can be avoided by studying the long-range part of the correlation function, which is typically chosen to be $|\Delta\eta| > 2$. Because the dijet contribution to the two-particle correlation function is not localized in $\Delta\eta$, that contribution has to be subtracted from the measured correlation function, typically using the correlation function measured in low-multiplicity ("peripheral") events. Different peripheral subtraction methods have been applied for the p+Pb measurements

[2] See [52, 53] for analyses of the breakdown of factorization.

in the literature [2, 4]; all of them relied on the "zero yield at minimum" (ZYAM) [2, 4] hypothesis to subtract an assumed flat combinatoric component from the peripheral reference correlation function. These methods were found to be inadequate for pp collisions where the amplitude of the dijet enhancement at $\Delta\phi = \pi$ is much larger than the (absolute) amplitude of the sinusoidal modulation. For the measurements in Ref. [41], a template-fitting method, described below, was developed that was better suited for extracting a small sinusoidal modulation from the data. Application of the template fitting method to the pp data provided an excellent description of the measured correlation functions. It also indicated substantial bias resulting from the application of the ZYAM-subtraction procedure to the peripheral reference correlation function due to the non-zero $v_{2,2}$ in low-multiplicity events. As a result, the measurements presented in Ref. [41] were obtained without using ZYAM subtraction. However, the previously published p+Pb data [4] may be susceptible to an unknown bias due to the use of the ZYAM method. Thus, a re-analysis of the p+Pb data is both warranted and helpful in making comparisons between pp and p+Pb data.

To address the points raised above, this note extends previous measurements of two-particle correlations in pp collisions at $\sqrt{s} = 13$ TeV using additional data acquired by ATLAS subsequent to the measurements in Ref. [41] and provides new measurements of such correlations in pp collisions at $\sqrt{s} = 5.02$ TeV. It also presents a re-analysis of two-particle correlations in 5.02 TeV p+Pb collisions and presents a direct comparison between the pp and p+Pb data at the same per-nucleon center-of-mass energy as well as a comparison between the pp data at the two energies. Two-particle Fourier coefficients $v_{n,n}$ are measured, where statistical precision allows, for $n = 2, 3$, and 4 as a function of charged particle multiplicity and transverse energy. Measurements are performed for different $p_{\mathrm{T}}^{\mathrm{a}}$ and $p_{\mathrm{T}}^{\mathrm{b}}$ intervals and the factorization of the resulting $v_{n,n}$ values is tested.

This note is organized as follows. Section 2 gives a brief overview of the ATLAS detector sub-systems and triggers used in this analysis. Section 3 describes the data sets, and the offline selection criteria used to select events and reconstructed charged-particle tracks. The variables used to characterize the "event-activity" of the pp and p+Pb collisions are also described. Section 4 gives details of the two-particle correlation method. Section 5 describes the template fitting of the two-particle correlations, which was originally developed in Ref. [41]. The template fits are used to extract the Fourier harmonics, $v_{n,n}$ (Eq. (2)), of the long-range correlation, and the factorization of the $v_{n,n}$ into single-particle harmonics v_n (Eq. (3)) is studied. The stability of the $v_{n,n}$ to the relative pseudorapidity separation between, the charged-particle pairs is also checked. Section 6 describes the systematic uncertainties associated with the measured $v_{n,n}$. In Sec. 7 the main results of the analysis, which are the p_{T} and event activity dependence of the single particle harmonics, v_n, are presented. Detailed comparisons of the v_n between the three data sets: 13 TeV pp, 5.02 TeV pp, and 5.02 TeV p+Pb are also shown. Section 8 gives a summary of the main results and observations.

2 Experiment

2.1 ATLAS detector

The measurements presented in this note have been performed using the ATLAS [54] inner detector (ID), minimum-bias trigger scintillators (MBTS), calorimeter, zero-degree calorimeters (ZDC), and the trigger and data acquisition systems. The ID detects charged particles within $|\eta|<2.5$[3] using a combination of

[3] ATLAS uses a right-handed coordinate system with its origin at the nominal interaction point (IP) in the center of the detector and the z-axis along the beam pipe. The x-axis points from the IP to the center of the LHC ring, and the y-axis points

pp 13 TeV		pp 5 TeV		p+Pb	
L1	HLT	L1	HLT	L1	HLT
MBTS	$N_{\mathrm{trk}}^{\mathrm{HLT}} \geq 60$	$E_{\mathrm{T}}^{\mathrm{L1}} > 5$ GeV	$N_{\mathrm{trk}}^{\mathrm{HLT}} \geq 60$	$E_{\mathrm{T}}^{\mathrm{L1,FCal}} > 10$ GeV	$N_{\mathrm{trk}}^{\mathrm{HLT}} \geq 100$
$E_{\mathrm{T}}^{\mathrm{L1}} > 10$ GeV	$N_{\mathrm{trk}}^{\mathrm{HLT}} \geq 90$	$E_{\mathrm{T}}^{\mathrm{L1}} > 10$ GeV	$N_{\mathrm{trk}}^{\mathrm{HLT}} \geq 90$	$E_{\mathrm{T}}^{\mathrm{L1,FCal}} > 10$ GeV	$N_{\mathrm{trk}}^{\mathrm{HLT}} \geq 130$
		$E_{\mathrm{T}}^{\mathrm{L1}} > 20$ GeV	$N_{\mathrm{trk}}^{\mathrm{HLT}} \geq 90$	$E_{\mathrm{T}}^{\mathrm{L1,FCal}} > 50$ GeV	$N_{\mathrm{trk}}^{\mathrm{HLT}} \geq 150$
				$E_{\mathrm{T}}^{\mathrm{L1,FCal}} > 50$ GeV	$N_{\mathrm{trk}}^{\mathrm{HLT}} \geq 180$
				$E_{\mathrm{T}}^{\mathrm{L1,FCal}} > 65$ GeV	$N_{\mathrm{trk}}^{\mathrm{HLT}} \geq 200$
				$E_{\mathrm{T}}^{\mathrm{L1,FCal}} > 65$ GeV	$N_{\mathrm{trk}}^{\mathrm{HLT}} \geq 225$

Table 1: The list of L1 and $N_{\mathrm{trk}}^{\mathrm{HLT}}$ requirements for the pp and p+Pb HMT triggers used in this analysis. For the pp HMT triggers, the L1 requirement is on the E_{T} over the entire ATLAS calorimetry ($E_{\mathrm{T}}^{\mathrm{L1}}$) or hits in the MBTS. For the p+Pb HMT triggers, the L1 requirement is on the E_{T} restricted to the FCal ($E_{\mathrm{T}}^{\mathrm{L1,FCal}}$).

silicon pixel detectors including the "Insertable B–layer" (IBL) [55, 56] that was installed between Run 1 and Run 2, silicon micro-strip detectors (SCT), and a straw-tube transition radiation tracker (TRT), all immersed in a 2 T axial magnetic field [57]. The MBTS system detects charged particles over $2.07 < |\eta| < 3.86$ using two hodoscopes positioned at $z = \pm 3.6$ m. These hodoscopes were rebuilt between Run 1 and Run 2. The ATLAS calorimeter system consists of a liquid argon (LAr) electromagnetic (EM) calorimeter covering $|\eta| < 3.2$, a steel–scintillator sampling hadronic calorimeter covering $|\eta| < 1.7$, a LAr hadronic calorimeter covering $1.5 < |\eta| < 3.2$, and two LAr electromagnetic and hadronic forward calorimeters (FCal) covering $3.2 < |\eta| < 4.9$. The ZDCs, situated ≈140 m from the nominal IP, detect neutral particles, mostly neutrons and photons, with $|\eta|>8.3$. The ZDCs use tungsten plates as absorbers, and quartz rods sandwiched between the tungsten plates as the active medium.

2.2 Trigger

The ATLAS trigger system [58] consists of a Level-1 (L1) trigger implemented using a combination of dedicated electronics and programmable logic, and a software-based high-level trigger (HLT). Due to the large interaction rates, only a small fraction of minimum-bias events could be recorded for all three data sets. The configuration of the minimum-bias (MB) triggers varied between the different data sets. Minimum-bias p+Pb events were selected by requiring a hit in at least one MBTS counter on each side (MBTS_1_1) or a signal in the ZDC on the Pb-fragmentation side with the trigger threshold set just below the peak corresponding to a single neutron. In the 13 TeV pp data, MB events were selected by a L1 trigger that requires a signal in at least one MBTS counter (MBTS_1). In the 5.02 TeV pp data, MB events were selected using the MBTS_1, MBTS_1_1, and a third trigger that required a minimum of one reconstructed track at the HLT. In order to enhance the number of events having high charged-particle multiplicity, several high-multiplicity (HMT) triggers were implemented. These apply a L1 requirement on either the transverse energy (E_{T}) in the calorimeters or on the number of hits in the MBTS, and an HLT requirement on the multiplicity of HLT-reconstructed charged particle tracks. That multiplicity, $N_{\mathrm{trk}}^{\mathrm{HLT}}$, is evaluated for tracks having $p_{\mathrm{T}}>0.4$ GeV that are associated with the reconstructed vertex with the highest multiplicity in the event. This last requirement suppresses the selection of events with multiple collisions (pileup), as long as the collision vertices are not so close as to be indistinguishable. The HMT trigger configurations used in this analysis are summarized in Table 1.

upward. Cylindrical coordinates (r, ϕ) are used in the transverse plane, ϕ being the azimuthal angle around the beam pipe. The pseudorapidity is defined in terms of the polar angle θ as $\eta = -\ln\tan(\theta/2)$.

3 Data sets

The $\sqrt{s}$ = 13 and 5.02 TeV pp data were collected during Run 2 of the LHC. The 13 TeV pp data were recorded over two periods: a set of low-luminosity runs in June 2015 (used in Ref. [41]) for which the collision rate per crossing, μ, varied between ~0.002 and ~0.04, and a set of intermediate-luminosity runs in August 2015 where the μ varied between 0.05 and 0.6. The 5.02 TeV pp data were recorded during November 2015 in a set of low-luminosity runs with μ ~1.5. The p+Pb data were recorded in Run 1 during p+Pb operation of the LHC in January 2013. During that period, the LHC was configured with a 4 TeV proton beam and a 1.57 TeV per-nucleon Pb beam that together produced collisions at $\sqrt{s_{\mathrm{NN}}}$=5.02 TeV. The higher energy of the proton beam produces a net rapidity shift of the nucleon–nucleon center-of-mass frame by 0.47 units in the proton-going direction, relative to the ATLAS rest frame. The p+Pb data were collected in two periods between which the directions of the proton and lead beams were reversed. The integrated luminosities used in this note are as follows: 75 nb^{-1} for the $\sqrt{s}$=13 TeV pp data, 28 pb^{-1} for the $\sqrt{s}$=5.02 TeV pp and 28 nb^{-1} for the $\sqrt{s_{\mathrm{NN}}}$=5.02 TeV p+Pb data.

3.1 Event and track selection

In the offline analysis, additional requirements are imposed on the events selected by the MB and HMT triggers. The events are required to have a reconstructed vertex with the z-position of the vertex restricted to ±150 mm. In the p+Pb data, non-collision backgrounds are suppressed by requiring at least one hit in a MBTS counter on each side of the interaction point, and the difference between times measured on the two sides of the MBTS to be less than 10 ns. In the 2013 p+Pb run, the luminosity conditions provided by the LHC result in an average probability of 3% for pileup events. The pileup events are suppressed by rejecting events containing more than one good reconstructed vertex. The remaining pileup events are further suppressed using the number of detected neutrons, N_n, measured in the ZDC on the Pb-fragmentation side. The distribution of N_n in events with pileup is broader than that for the events without pileup. Hence, rejecting events at the high tail-end of the ZDC signal distribution further suppresses the pileup, while retaining more than 98% of the events without pileup. In the pp data, pileup is suppressed by only using tracks associated with the vertex having the largest $\sum p_{\mathrm{T}}^2$, where the sum is over all tracks associated with the vertex.

In the p+Pb analysis, charged-particle tracks are reconstructed in the ID using an algorithm optimized for pp minimum-bias measurements [59]. The tracks are required to have p_{T} >0.4 GeV and $|\eta|$<2.5, at least one pixel hit, and the additional requirement of a hit in the first pixel layer when one is expected, [4] and at least six SCT hits. In addition, the transverse (d_0) and longitudinal ($z_0 \sin(\theta)$) impact parameters of the track relative to the vertex are required to be less than 1.5 mm. They are also required to satisfy $|d_0/\sigma_{d_0}|$<3 and $|z_0 \sin(\theta)/\sigma_z|$<3, where σ_{d_0} and σ_z are uncertainties on d_0 and $z_0 \sin(\theta)$ respectively.

In the pp analysis, charged-particle tracks and primary vertices are reconstructed in the ID using an algorithm similar to that used in Run 1, but substantially modified to improve performance [60, 61]. The reconstructed tracks are required to pass the following selection criteria: p_{T}>0.4 GeV and $|\eta|$<2.5; at least one pixel hit, with the additional requirement of a hit in the IBL if one is expected (if a hit is not expected in the IBL, a hit in the next pixel layer is required if such a hit is expected); a minimum of six hits in the SCT; $|d_0^{\mathrm{BL}}|$<1.5 mm, where the transverse impact parameter of the track, d_0^{BL}, is calculated with respect to the average beam position; and $|\Delta z_0 \sin(\theta)|$<1.5 mm, where z_0 is the longitudinal impact parameter, and

[4] A hit is expected if the extrapolated track crosses an active region of a pixel module that has not been disabled.

the difference is between the position of the track where d_0^{BL} is measured and the primary vertex. Finally, in order to remove tracks with mismeasured p_{T} due to interactions with the material or other effects, the track-fit χ^2 probability is required to be larger than 0.01 for tracks having $p_{\mathrm{T}} > 10$ GeV.

The efficiencies, $\epsilon(p_{\mathrm{T}}, \eta)$, of track reconstruction for the above track selection cuts are obtained using Monte Carlo generated events that are passed through a GEANT4 [62] simulation [63] of the ATLAS detector response and reconstructed using the algorithms applied to the data. For determining the p+Pb efficiencies, the events are generated with version 1.38b of the HIJING event generator [64] with a center-of-mass boost matching the beam conditions. For determining the pp efficiencies, non-diffractive 13 TeV pp events obtained from the Pythia 8 [65] event generator (A2 tune [66], MSTW2008LO PDFs [67]) are used. Both the pp and p+Pb efficiencies increase by ~3% from 0.4–0.6 GeV and vary only weakly with p_{T} for p_{T}>0.6 GeV. In the p+Pb case, the efficiency for p_{T}>0.6 GeV ranges from 82% at η=0 to 70% at $|\eta|$=2 and 60% at $|\eta|$>2.4. The efficiency is also found to vary by less than 2% over the multiplicity range used in the analysis. In the pp case, the efficiency for p_{T}>0.6 GeV ranges from 88–90% at η=0 to 77–80% at $|\eta|$=1.5 and 68–73% for $|\eta|$>2.0.

3.2 Event-activity classes

As with previous ATLAS long-range correlation analyses in p+Pb and pp [2, 4, 41] collisions, the event activity is quantified by $N_{\mathrm{ch}}^{\mathrm{rec}}$: the total number of reconstructed charged-particle tracks with p_{T}>0.4 GeV, passing the track selections discussed in Sec 3.1. For p+Pb collisions there is a direct correlation between $N_{\mathrm{ch}}^{\mathrm{rec}}$ and the number of participating nucleons in the Pb nucleus: events with larger $N_{\mathrm{ch}}^{\mathrm{rec}}$ values have, on average, a larger number of participating nucleons in the Pb nucleus and a smaller impact parameter. In this case, the concept of centrality used in A+A collisions is applicable, and in this note the terms "central" and "peripheral" are used to refer to events with large and small values of $N_{\mathrm{ch}}^{\mathrm{rec}}$ respectively. For pp collisions there may not be a correlation between $N_{\mathrm{ch}}^{\mathrm{rec}}$ and impact parameter. However, for convenience, but keeping this caveat in mind, the pp events with large and small $N_{\mathrm{ch}}^{\mathrm{rec}}$ are also termed as "central" and "peripheral" respectively.

Figure 1 shows the $N_{\mathrm{ch}}^{\mathrm{rec}}$ distributions for the three data sets used in this note. The discontinuities in the distributions result from the different HMT triggers, for which an offline requirement of $N_{\mathrm{ch}}^{\mathrm{rec}} > N_{\mathrm{trk}}^{\mathrm{HLT}}$ is applied. This requirement ensures that the HMT triggers are used only where the HLT trigger efficiency is close to being fully efficient.

The pp event-activity can also be quantified using the total transverse energy deposited in the FCal ($E_{\mathrm{T}}^{\mathrm{FCal}}$). This quantity has been used to determine the centrality in all ATLAS heavy-ion analyses. Using the $E_{\mathrm{T}}^{\mathrm{FCal}}$ to characterize the event-activity has the advantage that independent sets of particles are used to determine the event-activity and to measure the long-range correlations. Similarly in the p+Pb case, the event-activity can be characterized by the sum of transverse energy measured on the Pb-fragmentation side of the FCal ($E_{\mathrm{T}}^{\mathrm{FCal,Pb}}$) [2, 4]. Results presented in this note use both $N_{\mathrm{ch}}^{\mathrm{rec}}$ and the $E_{\mathrm{T}}^{\mathrm{FCal}}$ (or $E_{\mathrm{T}}^{\mathrm{FCal,Pb}}$) to quantify the event-activity.

4 Two-particle correlation analysis

The study of two-particle correlations in this note follows previous ATLAS measurements in Pb+Pb [13, 68, 69], p+Pb [2, 4] and pp [41] collisions. For a given event class, the two-particle correlations are

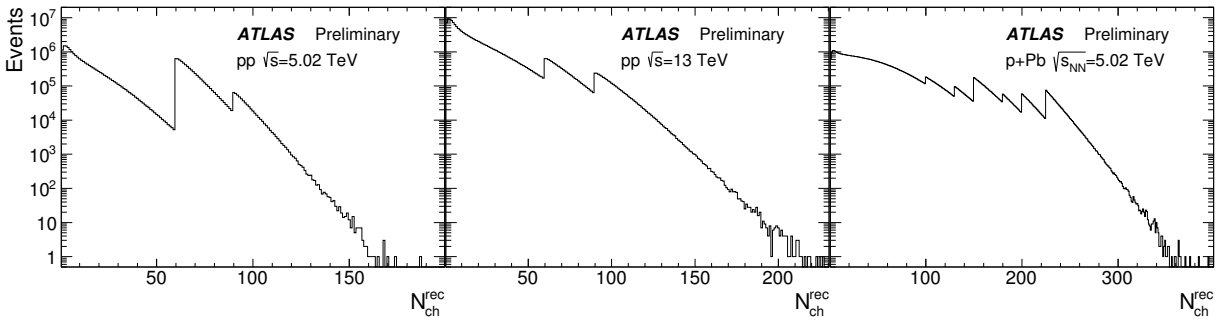

Figure 1: Distributions of the multiplicity, $N_{\mathrm{ch}}^{\mathrm{rec}}$, of reconstructed charged particles having p_{T} >0.4 GeV in the 5.02 TeV pp (left), 13 TeV pp, and 5.02 TeV p + Pb (right) data used in this analysis. The discontinuities in the distributions correspond to different high-multiplicity trigger thresholds.

measured as a function of the relative azimuthal angle $\Delta\phi \equiv \phi^a - \phi^b$ and pseudorapidity $\Delta\eta \equiv \eta^a - \eta^b$ separation. The labels a and b denote the two particles in the pair, which may be selected from different p_{T} intervals. The particles a and b are conventionally referred to as the "trigger" and "associated" particles, respectively. The correlation function is defined as:

$$C(\Delta\eta, \Delta\phi) = \frac{S(\Delta\phi, \Delta\eta)}{B(\Delta\phi, \Delta\eta)}\,, \tag{5}$$

where S and B represent pair distributions constructed from the same event and from "mixed events" [70], respectively. The same-event distribution, S, is constructed using all particle pairs that can be formed in each event from tracks that have passed the selections described in Sec. 3.1. The S contains both physical correlations between particle pairs, as well as correlations arising from detector acceptance effects. The mixed-event distribution, $B(\Delta\phi, \Delta\eta)$ is similarly constructed by choosing the two particles in the pair from different events. The B does not contain physical correlations, but is similarly affected by detector acceptance effects as S. In taking the ratio, S/B in Eq. (5), the detector acceptance effects largely cancel, and the resulting $C(\Delta\eta, \Delta\phi)$ contains physical correlations only. The pair of events used in the mixing are required to have similar $N_{\mathrm{ch}}^{\mathrm{rec}}$ ($|\Delta N_{\mathrm{ch}}^{\mathrm{rec}}|$<10) and similar z_{vtx} ($|\Delta z_{\mathrm{vtx}}|$<10 mm), so that acceptance effects in $S(\Delta\phi, \Delta\eta)$ are properly reflected in and compensated by corresponding variations in $B(\Delta\phi, \Delta\eta)$. To correct $S(\Delta\phi, \Delta\eta)$ and $B(\Delta\phi, \Delta\eta)$ for the individual ϕ-averaged inefficiencies of particles a and b, the pairs are weighted by the inverse product of their tracking efficiencies $1/(\epsilon_a\epsilon_b)$. Statistical uncertainties are calculated on $C(\Delta\eta, \Delta\phi)$ using standard error-propagation procedures assuming no correlation between S and B, and with the statistical variance on S and B in each $\Delta\eta$ and $\Delta\phi$ bin taken to be $\sum 1/(\epsilon_a\epsilon_b)^2$ where the sum runs over all of the pairs included in the bin. Typically, the two-particle correlations are used only to study the shape of the correlations in $\Delta\phi$, and are conveniently normalized. In this note, the normalization of $C(\Delta\eta, \Delta\phi)$ is chosen such that the $\Delta\phi$-averaged value of $C(\Delta\eta, \Delta\phi)$ is unity for $|\Delta\eta| > 2$.

Examples of correlation functions are shown in Fig. 2 for $0.5<p_{\mathrm{T}}^{\mathrm{a,b}}<5.0$ GeV and for two different $N_{\mathrm{ch}}^{\mathrm{rec}}$ ranges for each of the three data sets: 13 TeV pp (top), 5.02 TeV pp (middle), and 5.02 TeV p+Pb (bottom). The left panels show results for $0\leq N_{\mathrm{ch}}^{\mathrm{rec}}<20$ while the right panels show representative high-multiplicity ranges of $N_{\mathrm{ch}}^{\mathrm{rec}}\geq 120$ for the 13 TeV pp data, $90\leq N_{\mathrm{ch}}^{\mathrm{rec}}<100$ for the 5.02 TeV pp data and $N_{\mathrm{ch}}^{\mathrm{rec}}\geq 220$ for the 5.02 TeV p+Pb data. The correlation functions are plotted over the range $-\pi/2<\Delta\phi<3\pi/2$; the periodicity of the measurement requires that $C(\Delta\eta, 3\pi/2)=C(\Delta\eta, -\pi/2)$. The low-multiplicity correlation functions exhibit features that are understood to result primarily from hard-scattering processes: a peak centered at $\Delta\eta=\Delta\phi=0$ that arises primarily from jets and an enhancement centered at $\Delta\phi=\pi$ and extending over the full $\Delta\eta$ range that results from dijets. These features also dominate the high-multiplicity

correlation functions. Additionally, in the high-multiplicity correlation functions, each of the three systems exhibit a ridge – an enhancement centered at $\Delta\phi$=0 that extends over the entire measured $\Delta\eta$ range.

One-dimensional correlation functions, $C(\Delta\phi)$, are obtained by integrating the numerator and denominator of Eq. (5) over $2<|\Delta\eta|<5$ prior to taking the ratio:

$$C(\Delta\phi) = \frac{\int_2^5 \mathrm{d}|\Delta\eta|\; S(\Delta\phi, |\Delta\eta|)}{\int_2^5 \mathrm{d}|\Delta\eta|\; B(\Delta\phi, |\Delta\eta|)} \equiv \frac{S(\Delta\phi)}{B(\Delta\phi)}. \tag{6}$$

This $|\Delta\eta|$ range is chosen to focus on the long-range features of the correlation functions. From the one-dimensional correlation functions, "per-trigger-particle yields," $Y(\Delta\phi)$ are calculated [2, 4, 70]:

$$Y(\Delta\phi) = \left(\frac{\int B(\Delta\phi)\mathrm{d}\Delta\phi}{N^a \int \mathrm{d}\Delta\phi} \right) C(\Delta\phi), \tag{7}$$

where N^a denotes the total number of trigger-particles, corrected to account for the tracking efficiency. The $Y(\Delta\phi)$ is identical in shape to $C(\Delta\phi)$, but has a physically relevant normalization: it represents the average number of associated particles per trigger-particle in a given $\Delta\phi$ interval. This allows operations, such as subtraction of the $Y(\Delta\phi)$ in an event-activity class from the $Y(\Delta\phi)$ in another, which have been used in studying the p+Pb ridge [2, 4].

5 Template fitting

In order to separate the ridge from other sources of angular correlations, such as dijets, ATLAS developed a template fitting procedure in Ref. [41]. In this procedure, the measured $Y(\Delta\phi)$ distributions are assumed to result from a superposition of a "peripheral" $Y(\Delta\phi)$ distribution, $Y^{\mathrm{periph}}(\Delta\phi)$, scaled up by a multiplicative factor and a constant modulated by $\cos(n\Delta\phi)$ for $n \geq 2$. The resulting template fit function,

$$Y^{\mathrm{templ}}(\Delta\phi) = F\, Y^{\mathrm{periph}}(\Delta\phi) + Y^{\mathrm{ridge}}(\Delta\phi)\,, \tag{8}$$

where

$$Y^{\mathrm{ridge}}(\Delta\phi) = G\left(1 + \sum_{n=2}^{\infty} 2v_{n,n}\cos\left(n\Delta\phi\right)\right), \tag{9}$$

has free parameters F and $v_{n,n}$. The coefficient, G, which represents the magnitude of the combinatoric component of $Y^{\mathrm{ridge}}(\Delta\phi)$, is fixed by requiring that $\int_0^\pi \mathrm{d}\Delta\phi\; Y^{\mathrm{templ}} = \int_0^\pi \mathrm{d}\Delta\phi\; Y$. In this note, when studying the $N_{\mathrm{ch}}^{\mathrm{rec}}$ dependence of the long-range correlation, the $0 \leq N_{\mathrm{ch}}^{\mathrm{rec}} < 20$ multiplicity interval is used to produce the $Y^{\mathrm{periph}}(\Delta\phi)$. When studying the $E_{\mathrm{T}}^{\mathrm{FCal}}$ ($E_{\mathrm{T}}^{\mathrm{FCal,Pb}}$) dependence, the $E_{\mathrm{T}}^{\mathrm{FCal}}$ <10 GeV ($E_{\mathrm{T}}^{\mathrm{FCal,Pb}}$ <10 GeV) interval is used to produce the $Y^{\mathrm{periph}}(\Delta\phi)$.

The template fitting procedure is similar to the peripheral subtraction procedure used in previous ATLAS p+Pb ridge analyses [4]. In those analyses, the scale factor for the peripheral reference, analogous to F in Eq. (8), was determined by matching the near-side jet peaks between the peripheral and central samples. A more important difference, however, lies in the treatment of the peripheral bin. In the earlier analyses, a ZYAM procedure was performed on the peripheral reference, and only the modulated part of the $Y^{\mathrm{periph}}(\Delta\phi)$, $Y^{\mathrm{periph}}(\Delta\phi) - Y^{\mathrm{periph}}(0)$, was used in the peripheral subtraction.[5] The ZYAM procedure

[5] The minimum of $Y^{\mathrm{periph}}(\Delta\phi)$ is at $\Delta\phi$=0 and is thus equal to $Y^{\mathrm{periph}}(0)$, which the ZYAM procedure subtracts out.

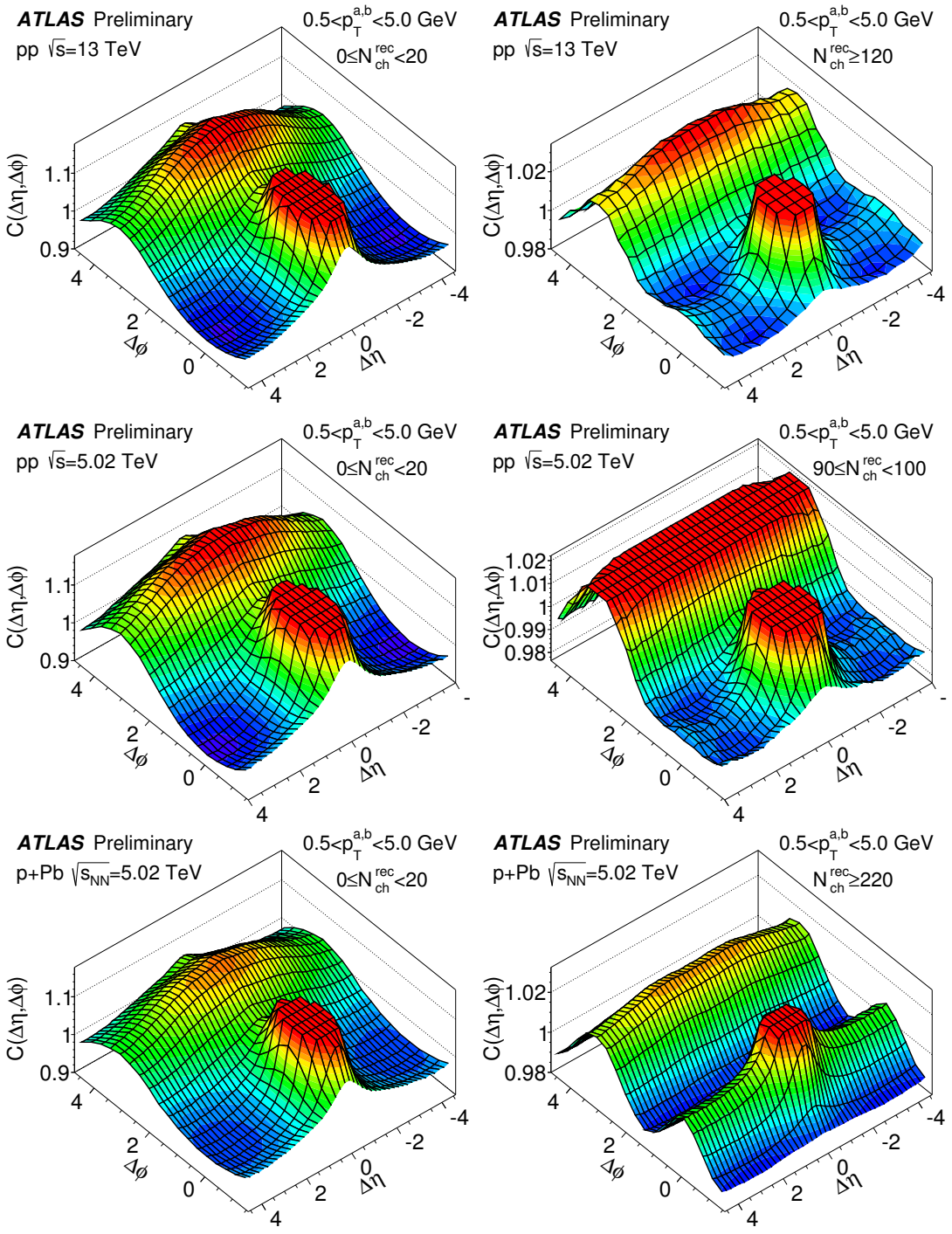

Figure 2: Two-particle correlation functions, $C(\Delta\eta, \Delta\phi)$, in 13 TeV pp collisions (top panels), 5.02 TeV pp collisions (middle panels) and in 5.02 TeV p+Pb collisions (bottom panels). The left panels correspond to a lower-multiplicity range of $0 \leq N_{\mathrm{ch}}^{\mathrm{rec}} < 20$. The right panels correspond to higher multiplicity ranges of $N_{\mathrm{ch}}^{\mathrm{rec}} \geq 120$ for 13 TeV pp, $90 \leq N_{\mathrm{ch}}^{\mathrm{rec}} < 100$ for the 5.02 TeV pp and $N_{\mathrm{ch}}^{\mathrm{rec}} \geq 220$ for the 5.02 TeV p+Pb. The plots are for charged particles having $0.5 < p_{\mathrm{T}}^{\mathrm{a,b}} < 5.0$ GeV. The distributions have been truncated to suppress the peak at $\Delta\eta = \Delta\phi = 0$ and are plotted over $|\Delta\eta| < 4.6$ ($|\Delta\eta| < 4.0$ for middle row) to avoid statistical fluctuations at larger $|\Delta\eta|$. For the middle-right panel, the peak at $\Delta\phi = \pi$ has also been truncated.

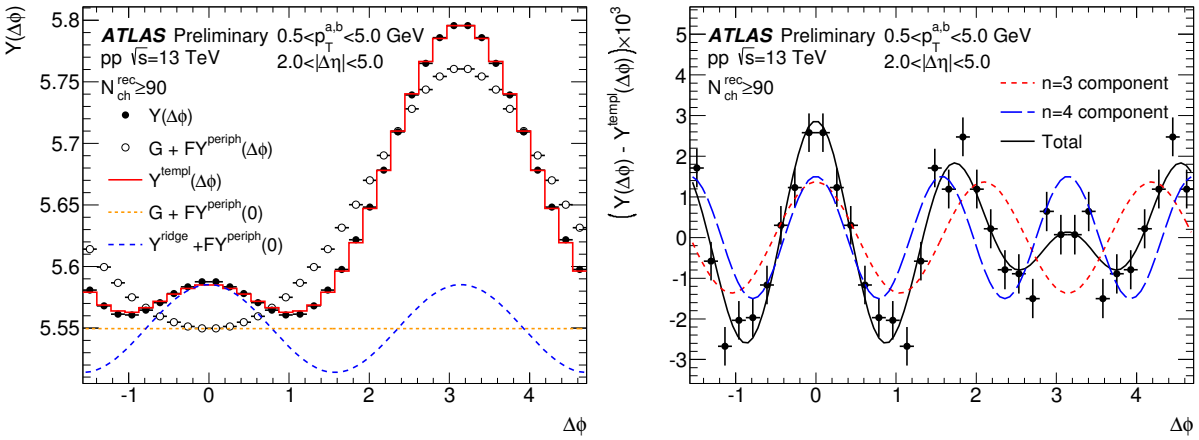

Figure 3: Left Panel: template fit to the the per-trigger particle yields, $Y(\Delta\phi)$, in 13 TeV pp collisions for charged particle pairs with $0.5<p_{\mathrm{T}}^{\mathrm{a,b}}<5$ GeV and $2<|\Delta\eta|<5$. This plot corresponds to the $N_{\mathrm{ch}}^{\mathrm{rec}}\geq 90$ multiplicity range. The template fitting includes only the 2$^{\mathrm{nd}}$ order harmonic, $v_{2,2}$. Right Panel: The difference between the $Y(\Delta\phi)$ and the template fit, showing the presence of $v_{3,3}$ and $v_{4,4}$ components. The vertical error bars indicate statistical uncertainties.

makes several assumptions, the most relevant of which for the present analysis is that there is no long-range correlation in the peripheral bin. As pointed out in Ref. [41], neglecting the non-zero modulation present in $Y^{\mathrm{periph}}(\Delta\phi)$ significantly biases the measured $v_{n,n}$ values. Results from an alternative version of the template fitting, where a ZYAM procedure is performed on the peripheral reference, by using $Y^{\mathrm{periph}}(\Delta\phi) - Y^{\mathrm{periph}}(0)$ in place of $Y^{\mathrm{periph}}(\Delta\phi)$ in Eq. (8), are also presented in this note. This ZYAM-based template fit is similar to the p+Pb peripheral subtraction procedure. These results are included mainly to compare with previous measurements and to demonstrate the improvements obtained using the present method.

In Ref. [41] the template fitting procedure only included the second-order harmonic $v_{2,2}$, but was able to well reproduce the $N_{\mathrm{ch}}^{\mathrm{rec}}$ dependent evolution of the $Y(\Delta\phi)$ on both the near and away sides. The left panel of Fig. 3 shows such a template fit, in the 13 TeV pp data, that only includes $v_{2,2}$. The right panel shows the difference between the $Y(\Delta\phi)$ and the $Y^{\mathrm{templ}}(\Delta\phi)$ demonstrating the presence of small (compared to $v_{2,2}$), but significant residual $v_{3,3}$ and $v_{4,4}$ components. While it is possible that $\cos 3\Delta\phi$ and $\cos 4\Delta\phi$ contributions could arise in the template fitting method due to small multiplicity-dependent changes in the shape of the dijet component of the correlation function, such effects would not produce the excess at $\Delta\phi\sim 0$ observed in the right-hand panel in Fig. 3. That excess and the fact that its magnitude is compatible with the remainder of the distribution indicates that there is real $\cos 3\Delta\phi$ and $\cos 4\Delta\phi$ modulation in the two-particle correlation functions. Thus, in this note the $v_{2,2}$ results in Ref. [41] have been extended to include $v_{3,3}$ and $v_{4,4}$ as well. A study of these higher order harmonics, including their $N_{\mathrm{ch}}^{\mathrm{rec}}$ and p_{T} dependence, and factorization (Eq. (4)) can help in better understanding the origin of the long-range correlations.

Figure 4 shows template fits to the 13 TeV (left panels) and 5.02 TeV pp data (right panels), for $0.5 < p_{\mathrm{T}}^{\mathrm{a,b}} < 5$ GeV. From top to bottom, each panel represents a different $N_{\mathrm{ch}}^{\mathrm{rec}}$ range. The template fits (Eq. (9)) include harmonics 2–4. Visually, a prominent ridge, i.e. a clear peak on the near-side, cannot be seen in the top two rows, which correspond to low and intermediate $N_{\mathrm{ch}}^{\mathrm{rec}}$ intervals, respectively. However, the template fits indicate the presence of a large modulated component of $Y^{\mathrm{ridge}}(\Delta\phi)$ even in these $N_{\mathrm{ch}}^{\mathrm{rec}}$

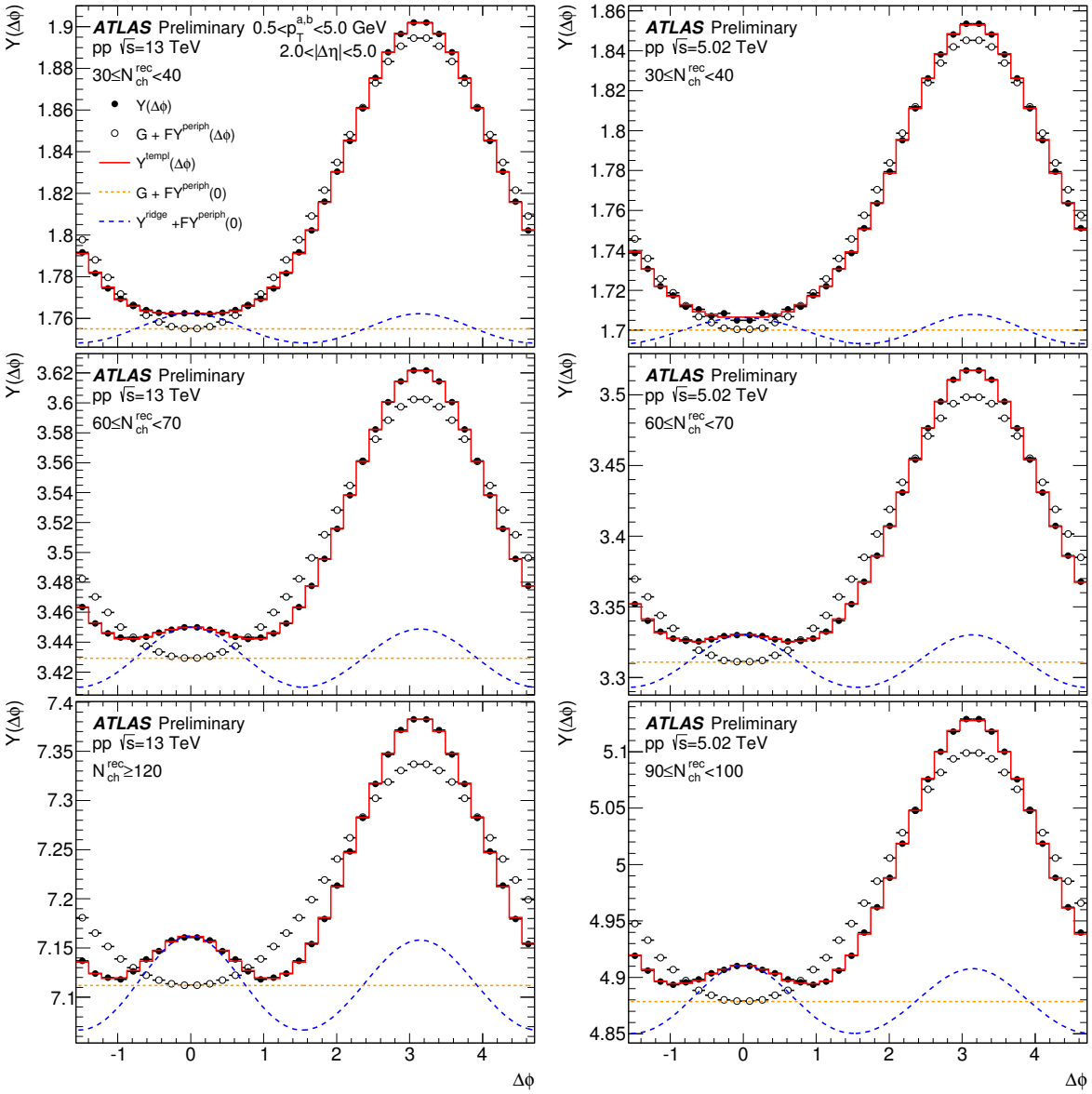

Figure 4: Template fits to the per-trigger particle yields $Y(\Delta\phi)$, in 13 TeV (left panels) and in 5.02 TeV pp collisions (right panels) for charged particle pairs with $0.5<p_{\mathrm{T}}^{\mathrm{a,b}}<5$ GeV and $2<|\Delta\eta|<5$. The template fitting includes 2$^{\mathrm{nd}}$, 3$^{\mathrm{rd}}$ and 4$^{\mathrm{th}}$ order harmonics. From top to bottom, each panel represents a different $N_{\mathrm{ch}}^{\mathrm{rec}}$ range. The solid points indicate the measured $Y(\Delta\phi)$, the open points and curves show different components of the template (see legend) that are shifted along the y-axis, where necessary, for clarity.

intervals. Several prior pp ridge measurements rely on the ZYAM method [70, 71] to extract yields on the near-side [14, 15]. In these analyses, the yield of excess pairs in the ridge above the minimum of the $Y(\Delta\phi)$ distribution is considered to be the strength of the ridge. Figure 4 shows that such a procedure would give zero yields in low and intermediate multiplicity collisions where the minimum of $Y(\Delta\phi)$ occurs at $\Delta\phi\sim0$. In high multiplicity events, the ZYAM-based yields, while non-zero, are still underestimated.

Figure 5 shows the template fits to the p+Pb data in a format similar to Fig. 4. The template fits describe the data well across the entire $N_{\mathrm{ch}}^{\mathrm{rec}}$ range used in this note. Previous p+Pb ridge analyses used a peripheral

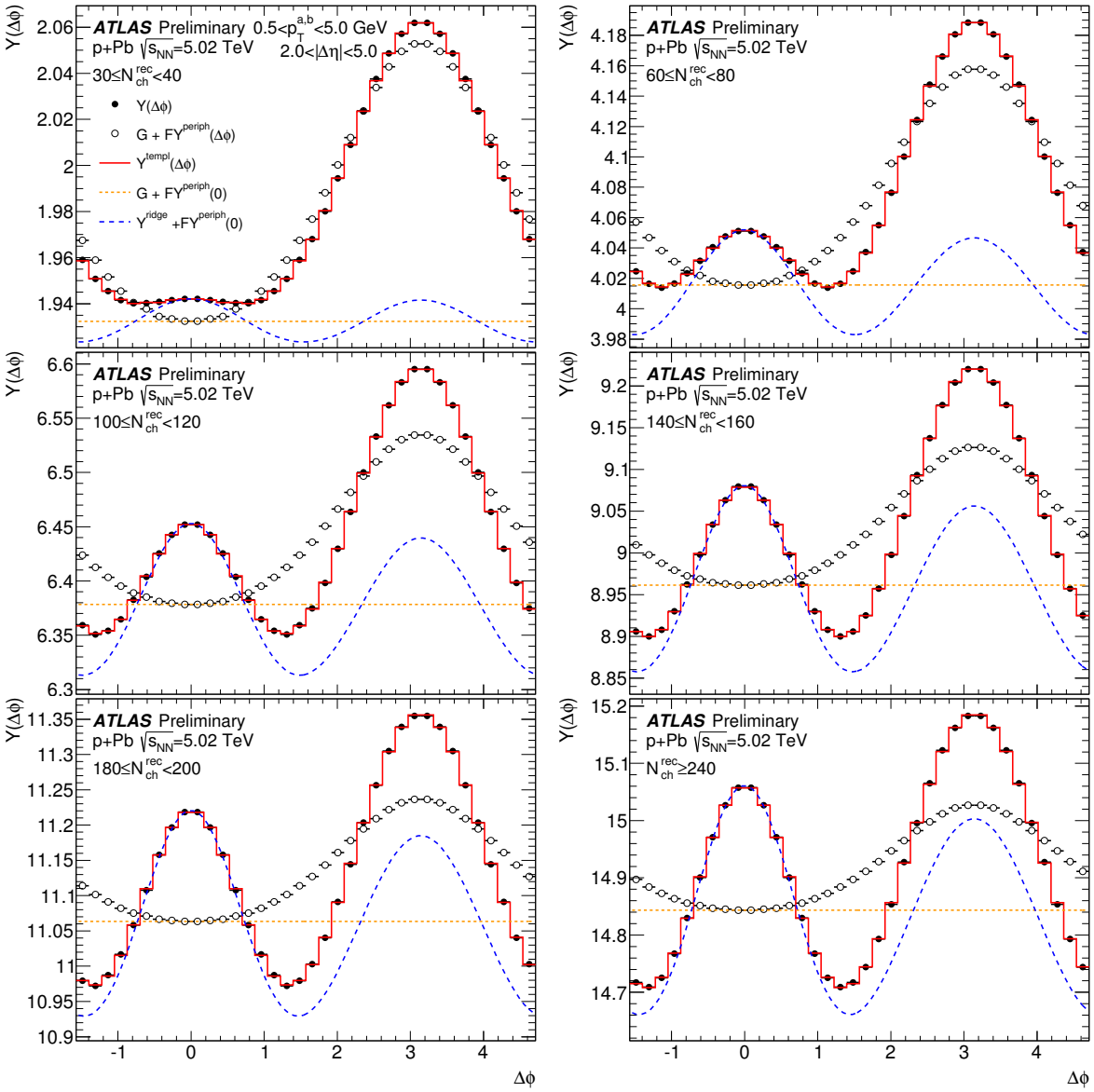

Figure 5: Template fits to the per-trigger particle yields $Y(\Delta\phi)$ in 5.02 TeV p+Pb collisions for charged particle pairs with $0.5<p_{\mathrm{T}}^{\mathrm{a,b}}<5$ GeV and $2<|\Delta\eta|<5$. The template fitting includes 2$^{\mathrm{nd}}$, 3$^{\mathrm{rd}}$ and 4$^{\mathrm{th}}$ order harmonics. Each panel represents a different $N_{\mathrm{ch}}^{\mathrm{rec}}$ range. The solid points indicate the measured $Y(\Delta\phi)$, the open points and curves show different components of the template (see legend) that are shifted along the y-axis, where necessary, for presentation.

subtraction procedure to remove the jet component from the $Y(\Delta\phi)$ [1]. That procedure is similar to the ZYAM-based template fitting procedure, in that it assumes absence of any long-range correlations in the peripheral events. In the next sections comparison between the $v_{n,n}$ obtained from these two methods will be shown.

5.1 Fourier coefficients

Figure 6 shows the $v_{n,n}$ obtained from the template fits in the 13 TeV pp data, as a function of $N_{\mathrm{ch}}^{\mathrm{rec}}$ and $E_{\mathrm{T}}^{\mathrm{FCal}}$. The $v_{n,n}$ from the ZYAM-based template fits as well as the coefficients obtained from a direct Fourier transform of the $Y(\Delta\phi)$ are also shown for comparison. While the template-$v_{n,n}$ are the most physically meaningful quantities, the Fourier-$v_{n,n}$ are also included to demonstrate how the template fitting removes the hard contribution. Similarly, the ZYAM-based template-$v_{n,n}$ are also included, as the ZYAM based fitting is similar to the peripheral subtraction procedure used in prior p+Pb analyses [2, 4], and comparing with the ZYAM-based results illustrates the improvement brought about in the template fitting procedure.

The $v_{2,2}$ values are nearly independent of $N_{\mathrm{ch}}^{\mathrm{rec}}$ throughout the measured range. As concluded in Ref. [41], this implies that the long-range correlation is not unique to high-multiplicity events, but is in fact present even at very low multiplicities. In the $E_{\mathrm{T}}^{\mathrm{FCal}}$ dependence, however, the $v_{2,2}$ shows a systematic decrease at low $E_{\mathrm{T}}^{\mathrm{FCal}}$. Further, the asymptotic values of the template-$v_{2,2}$ at large $N_{\mathrm{ch}}^{\mathrm{rec}}$ is also observed to be ~10% larger than the asymptotic value at large $E_{\mathrm{T}}^{\mathrm{FCal}}$. This might indicate that the $v_{2,2}$ at a given rapidity is more correlated with the local multiplicity than the global multiplicity.

The removal of the hard contribution to the $v_{2,2}$ in the template fitting can be seen by comparing to the Fourier-$v_{2,2}$ values. The Fourier-$v_{2,2}$ values are always larger than the template-$v_{2,2}$ and show a systematic increase at small $N_{\mathrm{ch}}^{\mathrm{rec}}$ ($E_{\mathrm{T}}^{\mathrm{FCal}}$). This indicates the presence of a relatively large contribution from back-to-back dijets over this range. Asymptotically, at large $N_{\mathrm{ch}}^{\mathrm{rec}}$ the Fourier-$v_{2,2}$ values become stable, but show a small decreasing trend in the $E_{\mathrm{T}}^{\mathrm{FCal}}$ dependence. The ZYAM-based $v_{2,2}$ values are smaller than the template-$v_{2,2}$ values for all $N_{\mathrm{ch}}^{\mathrm{rec}}$ ($E_{\mathrm{T}}^{\mathrm{FCal}}$), and by construction systematically decrease to zero for the lower $N_{\mathrm{ch}}^{\mathrm{rec}}$ ($E_{\mathrm{T}}^{\mathrm{FCal}}$) intervals. However, at larger $N_{\mathrm{ch}}^{\mathrm{rec}}$ ($E_{\mathrm{T}}^{\mathrm{FCal}}$) they too show only a weak dependence on the $N_{\mathrm{ch}}^{\mathrm{rec}}$ ($E_{\mathrm{T}}^{\mathrm{FCal}}$). Asymptotically, at large $N_{\mathrm{ch}}^{\mathrm{rec}}$ the values from the Fourier transform and from the default template fits match to within ~10% (relative). In general, the $v_{2,2}$ from all three methods agree within ±15% at large $N_{\mathrm{ch}}^{\mathrm{rec}}$ or $E_{\mathrm{T}}^{\mathrm{FCal}}$. This implies that at very high multiplicities, $N_{\mathrm{ch}}^{\mathrm{rec}} \sim 120$, the ridge signal is sufficiently strong that the assumptions made in removing the hard contributions to $Y(\Delta\phi)$ do not make a large difference. However, for the highest p_{T} values used in this analysis, $p_{\mathrm{T}}^{\mathrm{a}}$>7 GeV, it is observed that the width of the dijet peak in the pp correlation functions broadens with increasing multiplicity. This change is opposite that seen at lower p_{T} where the $v_{2,2}$ causes the dijet peak to become narrower. As a result, the measured $v_{2,2}$ values become negative. This bias from the multiplicity dependence of the hard-scattering contribution likely affects the correlation functions at lower $p_{\mathrm{T}}^{\mathrm{a,b}}$ values and its potential impact is discussed below.

The $v_{2,2}$ is the dominating component with, a magnitude ~30 times larger than $v_{3,3}$ and $v_{4,4}$, which are comparable to each other. This is in stark contrast to Pb+Pb collisions where in most central events, where the average geometry has less influence, the $v_{n,n}$ have comparable magnitudes [13]. The Fourier-$v_{3,3}$ shows considerable $N_{\mathrm{ch}}^{\mathrm{rec}}$ ($E_{\mathrm{T}}^{\mathrm{FCal}}$) dependence and is negative almost everywhere. However, the $v_{3,3}$ from the template fits are mostly positive. As the factorization of the $v_{n,n}$ requires that the $v_{n,n}$ be positive (Eq. (3)), the negative Fourier-$v_{3,3}$ clearly does not arise from single-particle modulation. However, because the template-$v_{3,3}$ is positive, its origin in from single-particle modulation cannot be ruled out. The $v_{4,4}$ from all three methods are positive throughout the measured $N_{\mathrm{ch}}^{\mathrm{rec}}$ range. Within statistical uncertainties, the $v_{4,4}$ is consistent with no $N_{\mathrm{ch}}^{\mathrm{rec}}$ or $E_{\mathrm{T}}^{\mathrm{FCal}}$ dependence.

Figure 7 shows the $v_{n,n}$ values from the 5.02 TeV pp data as a function of $N_{\mathrm{ch}}^{\mathrm{rec}}$ for a higher $p_{\mathrm{T}}^{\mathrm{a,b}}$ bin of 1.0–5 GeV. The same trends seen in the 13 TeV data (Fig. 6) are seen here, and the conclusions are identical

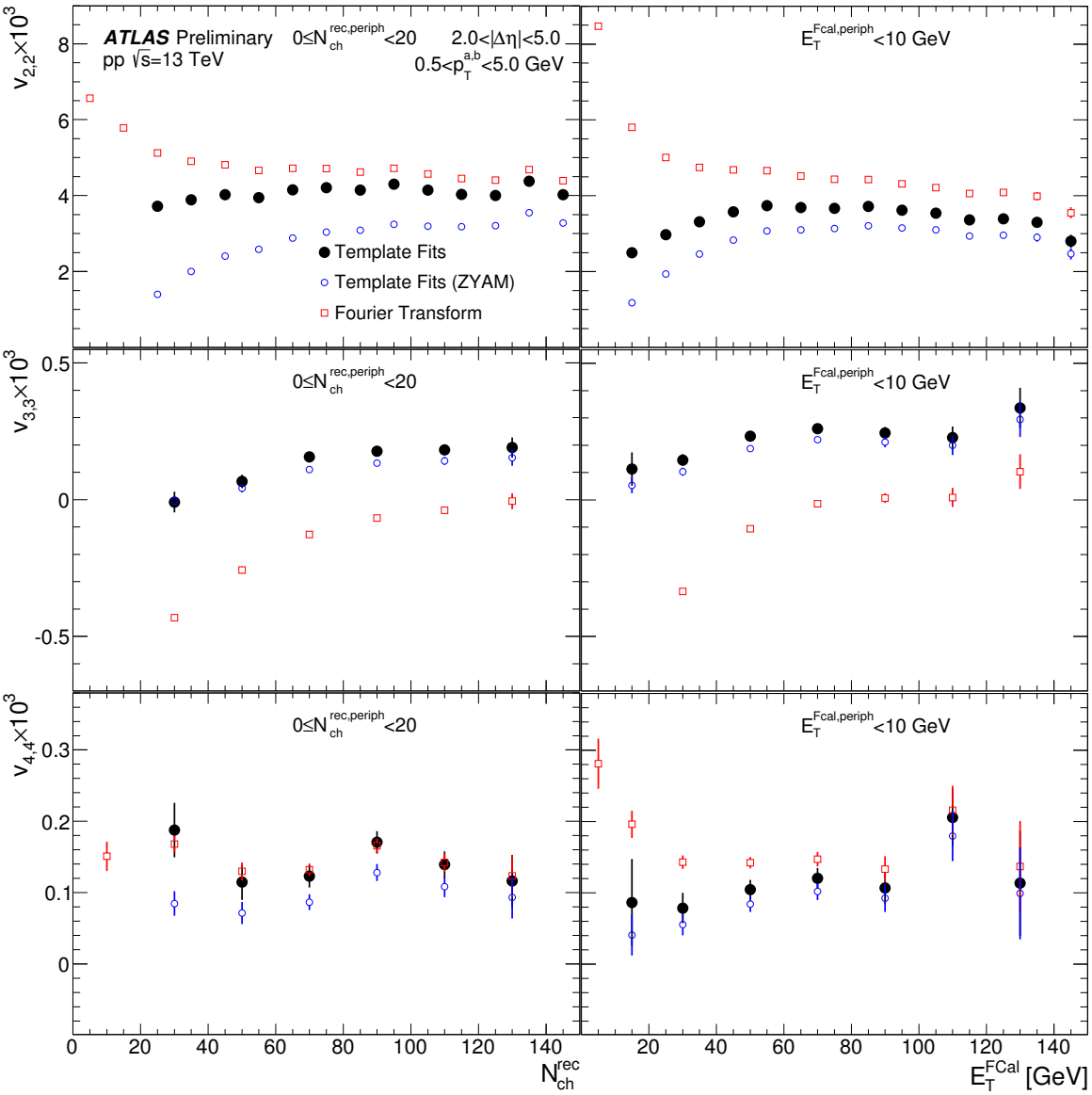

Figure 6: The $v_{n,n}$ obtained from the template fitting procedure in the 13 TeV pp data, as a function of $N_{\mathrm{ch}}^{\mathrm{rec}}$ (left panels), and as a function of the $E_{\mathrm{T}}^{\mathrm{FCal}}$ (right panels). The top, middle and bottom panels correspond to $v_{2,2}$, $v_{3,3}$, and $v_{4,4}$, respectively. The results are for $0.5<p_{\mathrm{T}}^{\mathrm{a,b}}<5$ GeV. The error bars indicate statistical uncertainties. The $v_{n,n}$ obtained from a direct Fourier transform of the $Y(\Delta\phi)$ and from the ZYAM-based template fits are also shown for comparison.

to those made in the 13 TeV case.

Figure 8 shows the $v_{n,n}$ for the p+Pb data. The results are plotted both as a function of $N_{\mathrm{ch}}^{\mathrm{rec}}$ (left panels) and $E_{\mathrm{T}}^{\mathrm{FCal,Pb}}$ (right panels). The $v_{2,2}$ obtained from the template fits shows a systematic increase with $N_{\mathrm{ch}}^{\mathrm{rec}}$ over $N_{\mathrm{ch}}^{\mathrm{rec}} \lesssim 150$, unlike the pp case where the $v_{2,2}$ is nearly independent of $N_{\mathrm{ch}}^{\mathrm{rec}}$. This is possibly indicative of a systematic change in the average collision geometry, which is present in p+Pb but not in pp collisions. A similar increase for the $v_{2,2}$ is also observed in the $E_{\mathrm{T}}^{\mathrm{FCal,Pb}}$ dependence. The higher order harmonics $v_{3,3}$ and $v_{4,4}$ show a stronger relative increase with increasing $N_{\mathrm{ch}}^{\mathrm{rec}}$ or $E_{\mathrm{T}}^{\mathrm{FCal,Pb}}$. This also

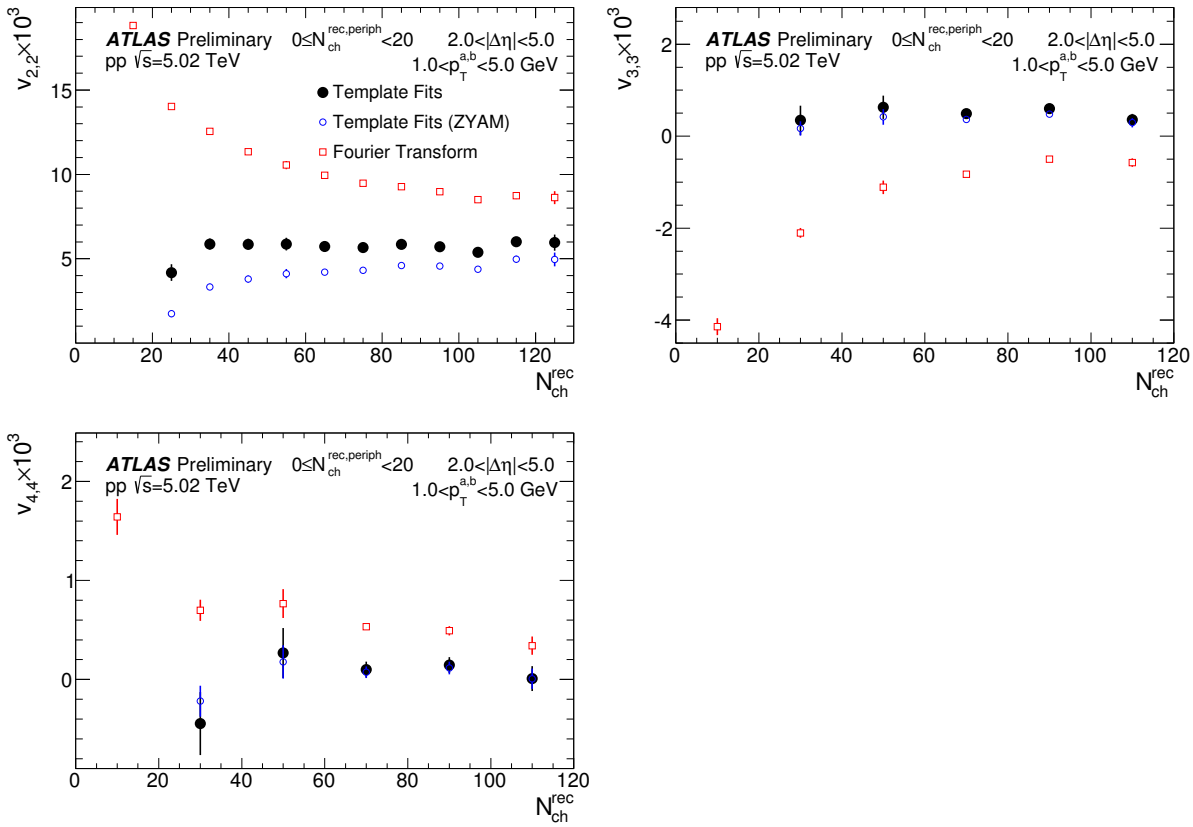

Figure 7: The $v_{n,n}$ obtained from the template fitting procedure in the 5.02 TeV pp data, as a function of $N_{\mathrm{ch}}^{\mathrm{rec}}$. The three panels correspond to n =2, 3, and 4, respectively. The results are for $1.0<p_{\mathrm{T}}^{\mathrm{a,b}}<5$ GeV. The error bars indicate statistical uncertainties. The $v_{n,n}$ obtained from a direct Fourier transform of the $Y(\Delta\phi)$ and from the ZYAM-based template fits are also shown for comparison.

implies that the assumption made in the template-fitting, regarding the independence or weak dependence of the $v_{n,n}$ on $N_{\mathrm{ch}}^{\mathrm{rec}}$, is not strictly correct for $v_{3,3}$ and $v_{4,4}$.

Figure 8 also compares the Fourier and ZYAM-based template-fit $v_{n,n}$ values. The $v_{n,n}$ from the peripheral subtraction procedure used in a previous ATLAS p+Pb long-range correlation analysis [4] are also shown. The peripheral-subtracted $v_{n,n}$ values are nearly identical to the values obtained from the ZYAM-based template-fits. This is not very surprising, as the treatment of the peripheral bin is identical in both cases: both use the ZYAM subtracted $Y^{\mathrm{periph}}(\Delta\phi)$ as the peripheral reference. What differs procedurally between the two methods is determination of the scale factor by which the $Y^{\mathrm{periph}}(\Delta\phi)$ is scaled up when subtracting it from the $Y(\Delta\phi)$. In the peripheral subtraction case, this scale factor, analogous to the parameter F in Eq. (8), is determined by matching the near-side jet peaks over the region $|\Delta\eta|<1$ and $|\Delta\phi|<1$. In the template fitting case, the parameter F is determined by the jet contribution to the away-side peak. The similarity of the $v_{2,2}$ from the two procedures implies that whether the matching is done in the near-side jet peak, or over the away-side peak, identical values of the scale factor are obtained. The Fourier-$v_{2,2}$ and template-fit-$v_{2,2}$ values are surprisingly similar except at very low $N_{\mathrm{ch}}^{\mathrm{rec}}$ or $E_{\mathrm{T}}^{\mathrm{FCal,Pb}}$. This is unlike the pp case (Figs. 6 and 7), where the two gave values that differed by ~15% (relative) at large $N_{\mathrm{ch}}^{\mathrm{rec}}$. This similarity does not hold for $v_{3,3}$ where the values from the template fit are systematically larger than the values obtained from Fourier decomposition. For all harmonics, the relative difference in the $v_{n,n}$

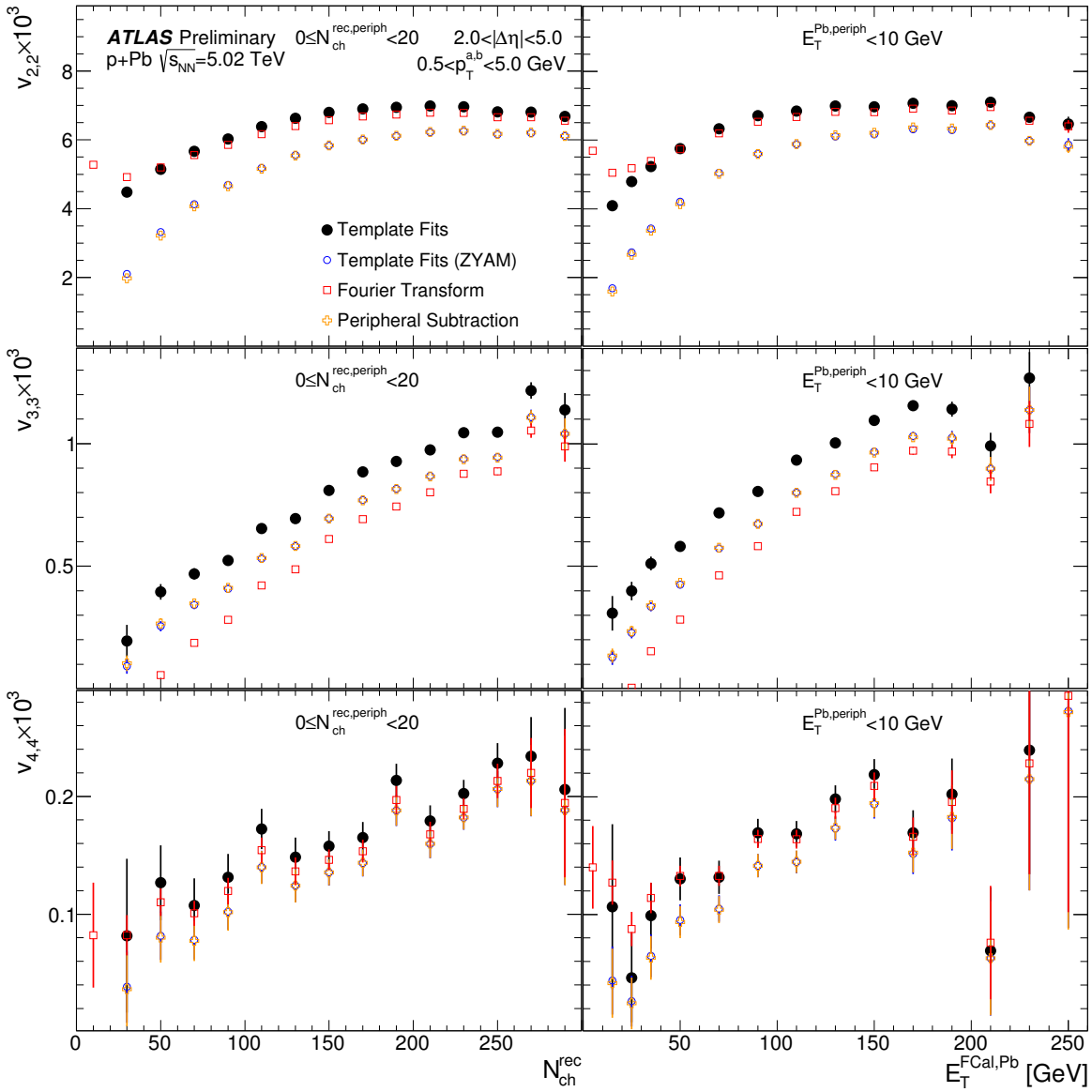

Figure 8: The $v_{n,n}$ obtained from the template fitting procedure in the 5.02 TeV p+Pb data, as a function of $N_{\mathrm{ch}}^{\mathrm{rec}}$ (left panels), and as a function of the Pb-going side FCal-E_{T} (right panels). The top, middle and bottom panels correspond to $v_{2,2}$, $v_{3,3}$, and $v_{4,4}$, respectively. The results are for $0.5<p_{\mathrm{T}}^{\mathrm{a,b}}<5$ GeV. The error bars indicate statistical uncertainties. The $v_{n,n}$ obtained from a direct Fourier transform of the $Y(\Delta\phi)$, the peripheral subtraction procedure, and from the ZYAM-based template fits are also shown for comparison.

decreases with increasing event-activity. Like in the pp case (Fig. 6), this implies that at large enough event activity, the $v_{n,n}$ are less sensitive to the assumptions made in removing the hard contributions.

5.2 Test of factorization in template fits

If the $v_{n,n}$ obtained from the template fits are the result of single-particle modulations, then the $v_{n,n}$ should factorize as Eq. (3), and the $v_n(p_{\mathrm{T}}^{\mathrm{a}})$ obtained by correlating trigger-particles at a given $p_{\mathrm{T}}^{\mathrm{a}}$ with associated

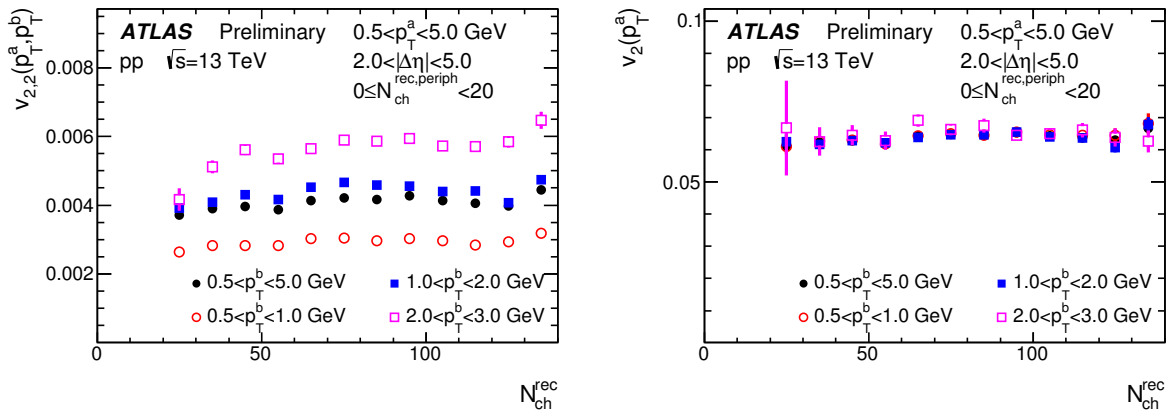

Figure 9: The left panel shows the $v_{2,2}$ as a function of $N_{\mathrm{ch}}^{\mathrm{rec}}$ in the 13 TeV pp data, for $0.5<p_{\mathrm{T}}^{\mathrm{a}}<5$ GeV and for several different choices of the $p_{\mathrm{T}}^{\mathrm{b}}$ interval. The right panel shows the corresponding v_2 values obtained using Eq. (4). The error bars indicate statistical uncertainties only.

particles in several different intervals of $p_{\mathrm{T}}^{\mathrm{b}}$ (Eq. (4)), should be independent of the choice of the $p_{\mathrm{T}}^{\mathrm{b}}$ interval. Figure 9 demonstrates the factorization of the $v_{2,2}$ in the 13 TeV pp data, as a function of $N_{\mathrm{ch}}^{\mathrm{rec}}$. The left panel shows the $v_{2,2}$ for $0.5<p_{\mathrm{T}}^{\mathrm{a}}<5$ GeV and for four different choices of the associated particle p_{T}: 0.5–5, 0.5–1, 1–2 and 2–3 GeV. The right panel shows the corresponding $v_2(p_{\mathrm{T}}^{\mathrm{a}})$ obtained using Eq. (4). While the $v_{2,2}(p_{\mathrm{T}}^{\mathrm{a}}, p_{\mathrm{T}}^{\mathrm{b}})$ values vary by a factor of ~2 between the different choices of the $p_{\mathrm{T}}^{\mathrm{b}}$ interval, the corresponding $v_2(p_{\mathrm{T}}^{\mathrm{a}})$ values agree quite well.Similar plots for the p+Pb data are shown in Fig. 10. Here due to larger statistical precision in the data, the factorization is tested for both $v_{2,2}$ and $v_{3,3}$. The variation in the $v_{2,2}(p_{\mathrm{T}}^{\mathrm{a}}, p_{\mathrm{T}}^{\mathrm{b}})$ between the four $p_{\mathrm{T}}^{\mathrm{b}}$ intervals is a factor of ~2 while the variation in the $v_{3,3}(p_{\mathrm{T}}^{\mathrm{a}}, p_{\mathrm{T}}^{\mathrm{b}})$ is more than a factor of 3. However, the corresponding $v_n(p_{\mathrm{T}}^{\mathrm{a}})$ values are in good agreement with each other, with the only exception being the $v_{2,2}$ for $2<p_{\mathrm{T}}^{\mathrm{b}}<3$ GeV where some breakdown is seen over the $N_{\mathrm{ch}}^{\mathrm{rec}}\lesssim 60$ range.

Figure 11 studies the $p_{\mathrm{T}}^{\mathrm{a}}$ dependence of the factorization in the 13 TeV pp data for $v_{2,2}$ (top panels) and $v_{3,3}$ (bottom panels). The results are shown for the $N_{\mathrm{ch}}^{\mathrm{rec}}\geq 90$ multiplicity range. The left panels show the $v_{n,n}$ as a function of $p_{\mathrm{T}}^{\mathrm{a}}$ for four different choices of the associated particle p_{T}: 0.5–5, 0.5–1, 1–2 and 2–3 GeV. The right panels show the corresponding v_n $(p_{\mathrm{T}}^{\mathrm{a}})$ obtained using Eq. (4). In the $v_{2,2}$ case, factorization holds reasonably well for $p_{\mathrm{T}}^{\mathrm{a}}\lesssim 3$ GeV, and becomes worse at higher p_{T}. This breakdown at higher p_{T} is likely caused by the above-discussed multiplicity-dependent distortions of the dijet component of the correlation function that are not accounted for in the template-fitting procedure. For $v_{3,3}$, the factorization holds reasonably well, for $p_{\mathrm{T}}^{\mathrm{b}}>1$ GeV. The $0.5<p_{\mathrm{T}}^{\mathrm{b}}<1$ GeV case shows a larger deviation in the factorization, but has much larger associated statistical uncertainties. Similar plots for the p+Pb case are shown in Fig. 12. Here the factorization holds for $v_{2,2}$, $v_{3,3}$ and $v_{4,4}$ up to p_{T}~5 GeV.

5.3 Dependence of $v_{n,n}$ on $\Delta\eta$ gap

A systematic study of the $\Delta\eta$ dependence of the $v_{n,n}$ can also help in determining the origin of the long-range correlation. If it arises from mechanisms that only correlate a few particles in an event, such as jets, then a strong dependence of the correlation on the $\Delta\eta$ gap between particle pairs is expected. Figure 13 shows the measured $v_{n,n}$ (left panels) and $v_n = \sqrt{v_{n,n}}$ (right panels), as a function of $|\Delta\eta|$ for $|\Delta\eta|>1$ in the

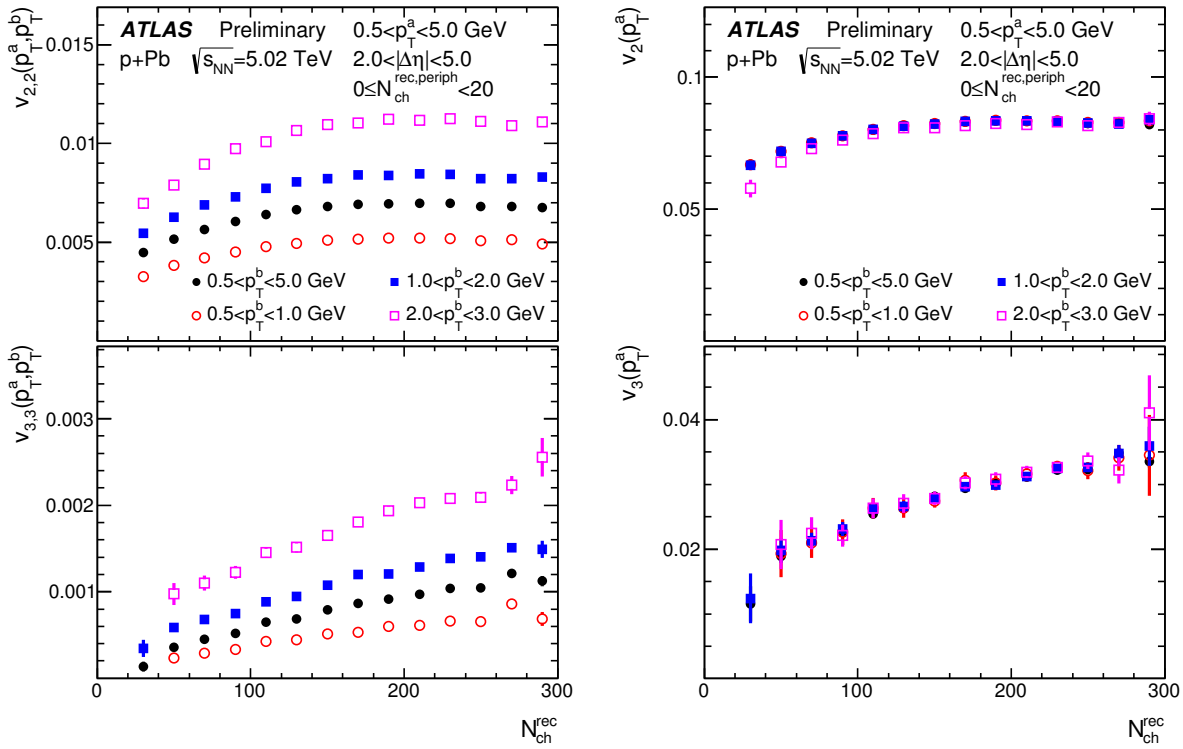

Figure 10: The left panels show the $v_{2,2}$ (top) and $v_{3,3}$ (bottom) as a function of $N_{\mathrm{ch}}^{\mathrm{rec}}$ in the 5.02 TeV p+Pb data, for $0.5<p_{\mathrm{T}}^{\mathrm{a}}<5$ GeV and for several different choices of the $p_{\mathrm{T}}^{\mathrm{b}}$ interval. The right panels shows the corresponding v_2 (top) and v_3 (bottom) values obtained using Eq. (4). The error bars indicate statistical uncertainties only.

13 TeV pp data. Also shown for comparison are the Fourier and ZYAM-based template-$v_{n,n}$. The $v_{2,2}$ (top left panel) and v_2 (top right panel) are quite stable, especially for $|\Delta\eta|>1.5$,where the influence of the near-side jet is diminished. In contrast, the Fourier-$v_{2,2}$ show a strong $|\Delta\eta|$ dependence. This is largest at small $|\Delta\eta|$ because of the presence of the sharply peaked near-side jet, but is considerable even for $|\Delta\eta|>2$. Similarly, the Fourier-$v_{3,3}$ shows large $|\Delta\eta|$ dependence, going from positive values at $|\Delta\eta|\sim1$ to negative values at large $|\Delta\eta|$, while the template-$v_{3,3}$ are only weakly changing in comparison. The Fourier-$v_{3,3}$ is often negative, ruling out the possibility of it being generated by single-particle anisotropies which requires that $v_{n,n} = v_n^2$ be positive. For points where the $v_{3,3}$ is negative, the v_3 is not defined and hence not plotted. The template-$v_{3,3}$ is, however, positive and, therefore, consistent with a single-particle anisotropy as its origin, except for the highest $|\Delta\eta|$ interval where it is consistent with zero. The $v_{4,4}$, like the $v_{2,2}$ and $v_{3,3}$ also only varies weakly with $|\Delta\eta|$. These observations further support the conclusion that the template-$v_{n,n}$ are coefficients of genuine long-range correlations.

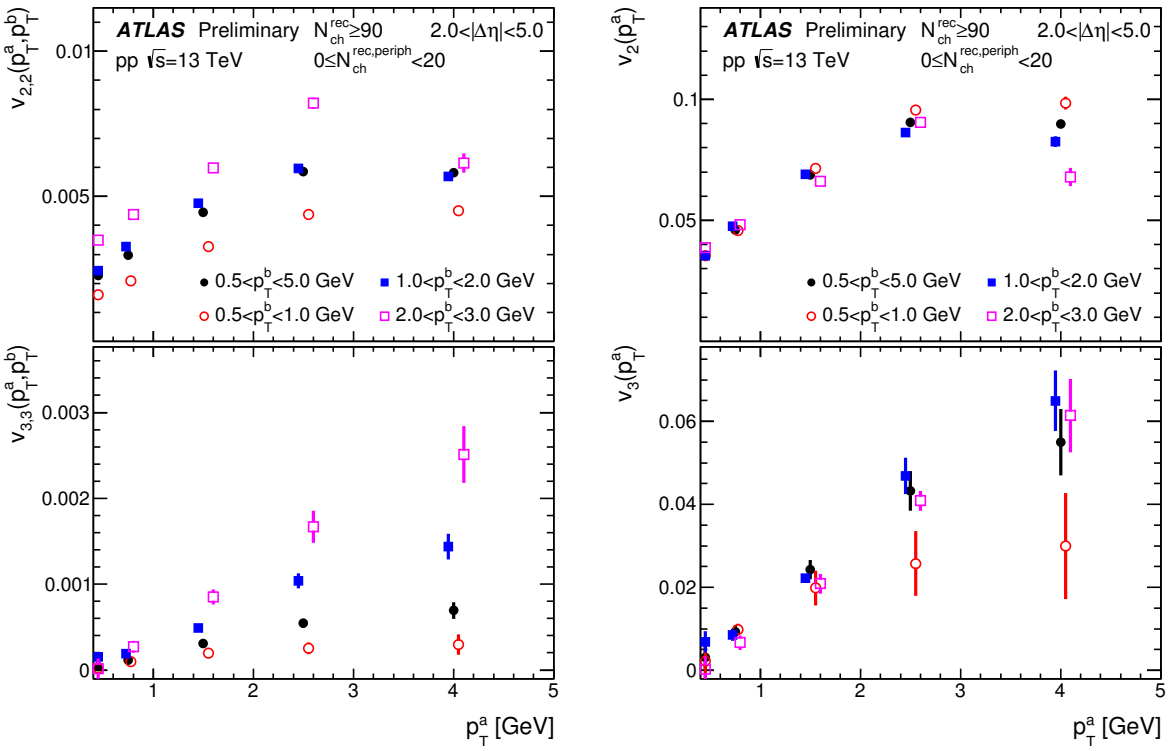

Figure 11: The left panels show the $v_{2,2}$ (top) and $v_{3,3}$ (bottom) as a function of $p_{\mathrm{T}}^{\mathrm{a}}$ in the 13 TeV pp data, for $N_{\mathrm{ch}}^{\mathrm{rec}}$ ≥90 and for several different choices of the $p_{\mathrm{T}}^{\mathrm{b}}$ interval. The right panels shows the corresponding v_2 (top) and v_3 (bottom) values obtained using Eq. (4). The error bars indicate statistical uncertainties only. The $p_{\mathrm{T}}^{\mathrm{a}}$ intervals plotted are 0.4–0.5, 0.5–1.0, 1–2, 2–3 and 3–5 GeV. In some cases, the data points have been slightly shifted along the x–axis, for clarity.

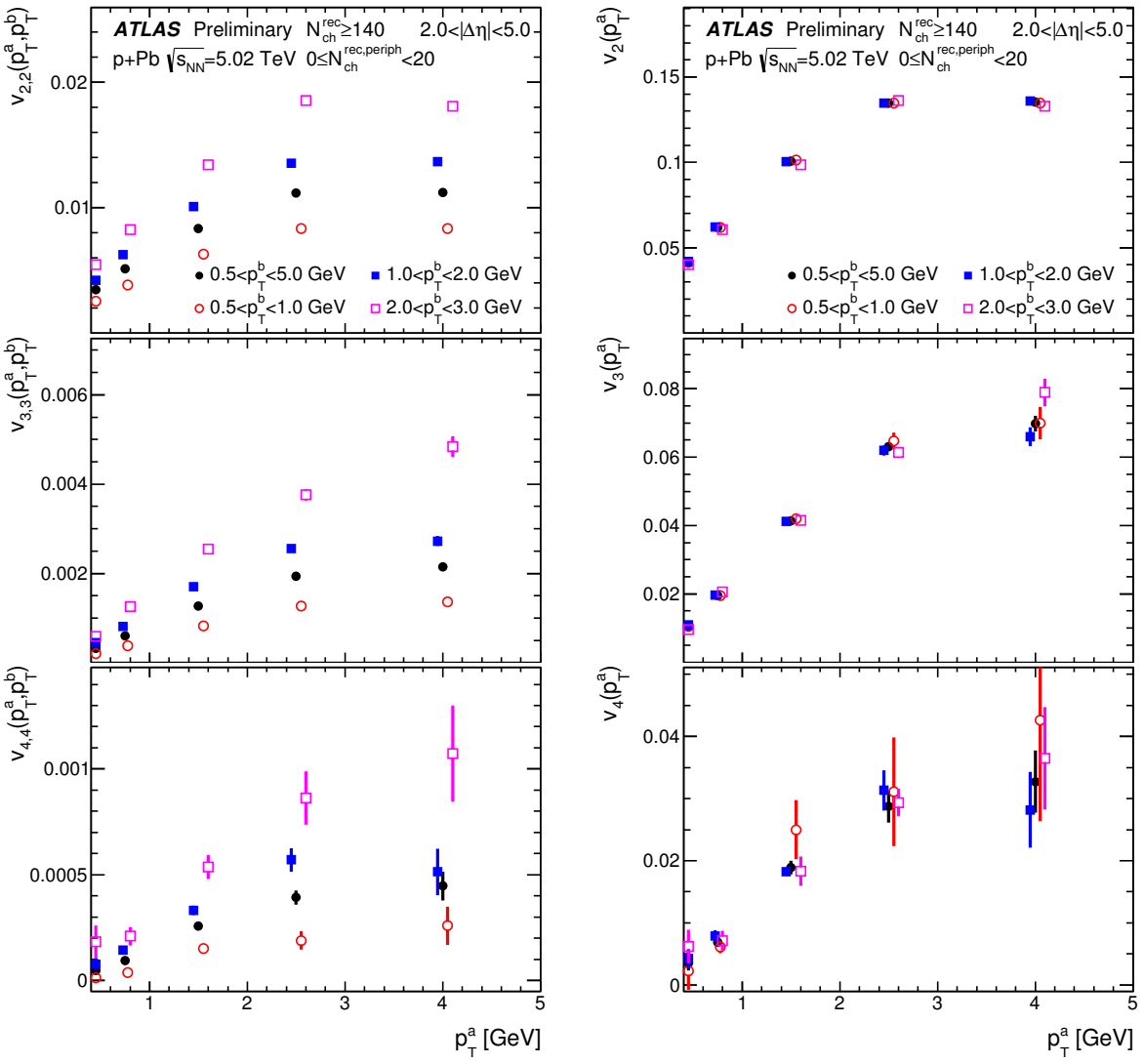

Figure 12: The left panels show the $v_{n,n}$ as a function of $p_{\mathrm{T}}^{\mathrm{a}}$ in the 5.02 TeV p+Pb data, for $N_{\mathrm{ch}}^{\mathrm{rec}}$ ≥140 and for several different choices of the $p_{\mathrm{T}}^{\mathrm{b}}$ interval. From top to bottom, the three rows correspond to n=2, 3 and 4. The right panels shows the corresponding v_n values obtained using Eq. (4). The error bars indicate statistical uncertainties only. The $p_{\mathrm{T}}^{\mathrm{a}}$ intervals plotted are 0.4–0.5, 0.5–1.0, 1–2, 2–3 and 3–5 GeV. In some cases, the data points have been slightly shifted along the x–axis, for clarity.

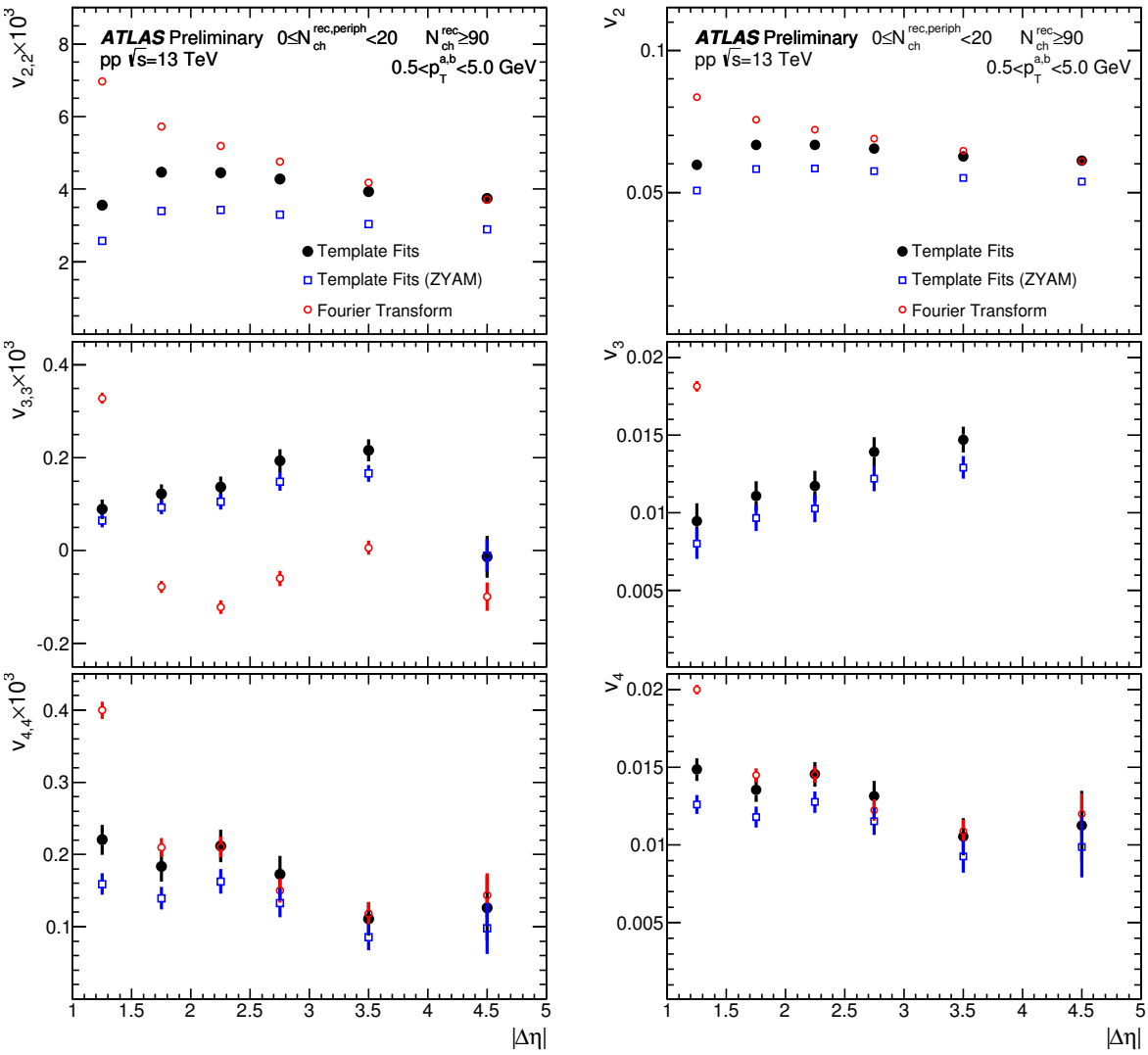

Figure 13: The $|\Delta\eta|$ dependence of the $v_{n,n}$ (left panels) and v_n (right panels) in the 13 TeV pp data. From top to bottom the rows correspond to n=2, 3 and 4 respectively. The ZYAM-template and Fourier-$v_{n,n}$ values are also shown for comparison. Only the range $|\Delta\eta|>1$ is shown to suppress the large Fourier-$v_{n,n}$ at $|\Delta\eta|\sim0$, that arise due to the near-side jet peak. Plots are for the $N_{\rm ch}^{\rm rec}\geq90$ multiplicity range and for $0.5<p_{\rm T}^{\rm a,b}<5$ GeV. The error bars indicate statistical uncertainties only.

6 Systematic uncertainties and cross-checks

The systematic uncertainties in this analysis arise from the tracking efficiency, choice of the peripheral bin used in the template fits, Monte Carlo consistency, pair acceptance and pileup. Each source is discussed separately below.

Peripheral interval: As explained in Sec. 5, the template fitting procedure makes two assumptions. First it assumes that the contributions to the $Y(\Delta\phi)$ from hard processes have identical shape across all event-activity ranges, and only change in overall scale. Second, it assumes that the $v_{n,n}$ are only weakly dependent on the event activity. The assumptions are self-consistent for the $N_{\rm ch}^{\rm rec}$ dependence of the $v_{n,n}$ in the 5.02 and 13 TeV pp data (left panels of Figs. 6–7), where the measured template-$v_{n,n}$ do turn out to be nearly independent of $N_{\rm ch}^{\rm rec}$. However, for the $E_{\rm T}^{\rm FCal}$ dependence in the pp data, and for both the $N_{\rm ch}^{\rm rec}$ and $E_{\rm T}^{\rm FCal,Pb}$ dependence in the p+Pb data, a systematic increase of the template-$v_{2,2}$ with event activity is seen at small event activity. This indicates the breakdown of one of the above two assumptions. To test the sensitivity of the measured $v_{n,n}$ to any residual changes in the width of the away-side jet peak and to the $v_{n,n}$ present in the peripheral reference, the analysis is repeated using 0–10 and 10–20 $N_{\rm ch}^{\rm rec}$ intervals to form $Y^{\rm periph}(\Delta\phi)$. The variation in the $v_{n,n}$ for the different choices of the peripheral interval are taken to be a systematic uncertainty.

The sensitivity of the template-v_2 to the choice of the peripheral interval is demonstrated in the left panels of Fig. 14, where the v_2 is shown for three different choices of the peripheral $N_{\rm ch}^{\rm rec}$ interval: 0–5, 0–10 and 0–20. In both the 13 TeV and 5.02 TeV pp data, except at very low $N_{\rm ch}^{\rm rec}$, the v_2 is nearly independent of the choice of the peripheral reference. In the 13 TeV pp case, the variation is ~6% at $N_{\rm ch}^{\rm rec}$~30 and decreases to ~1% for $N_{\rm ch}^{\rm rec}\geq$60. Even in the p+Pb case, where the measured template-$v_{2,2}$ exhibits some dependence on $N_{\rm ch}^{\rm rec}$, the dependence of the template-fit v_2 on the choice of the peripheral bin is quite small: ~6% at $N_{\rm ch}^{\rm rec}$~30 and decreases to ~2% for $N_{\rm ch}^{\rm rec}$~60. Also shown for comparison, are the corresponding v_2 values obtained from the ZYAM-based template fitting method (right panels of Fig. 14). These exhibit considerable dependence on the peripheral reference. For the 13 TeV pp case, the variation in the ZYAM-based v_2 is ~40% at $N_{\rm ch}^{\rm rec}$~30, and decreases to ~12% at $N_{\rm ch}^{\rm rec}$~60 and asymptotically at large $N_{\rm ch}^{\rm rec}$ is ~7%. For the p+Pb case, the variation is even larger: ~35% at $N_{\rm ch}^{\rm rec}$~30 and ~14% for $N_{\rm ch}^{\rm rec}$ ~60. These results show that the template-v_2 is quite stable to the choice of the peripheral interval, while the ZYAM-based result is very sensitive. This is one of the advantages of the new method.

Pileup: Pileup events, when included in the two-particle correlation measurement, dilute the $v_{n,n}$ signal as they produce pairs where the trigger and associated particle are from different collisions and thus have no physical correlations. The maximal fractional dilution in the $v_{n,n}$ is equal to the pileup rate. In the p+Pb data, nearly all of the events containing pileup are removed by the procedure described in Sec. 3. The influence of the residual pileup is evaluated by relaxing the pileup rejection criteria and then calculating the change in the $Y(\Delta\phi)$ and v_n values. The differences are taken as an estimate of the uncertainty for the $v_{n,n}$, and are found to be negligible in low event-activity classes, and increase to 4% for events with $E_{\rm T}^{\rm FCal,Pb}$~200 GeV or $N_{\rm ch}^{\rm rec}$~300.

In the pp data, for events containing multiple vertices, only tracks associated with the vertex having the largest $\sum p_{\rm T}^2$, where the sum is over all tracks associated with the vertex, are used in the analysis. Events containing multiple vertices where the vertices cannot be resolved, affect the results by increasing the combinatoric pedestal in $Y(\Delta\phi)$. The fraction of events with merged vertices is estimated and taken as the relative uncertainty associated with pileup in the pp analysis. This uncertainty is quite different, depending on whether it is studied as a function of $N_{\rm ch}^{\rm rec}$ or as function of $E_{\rm T}^{\rm FCal}$. The merged-vertex rate

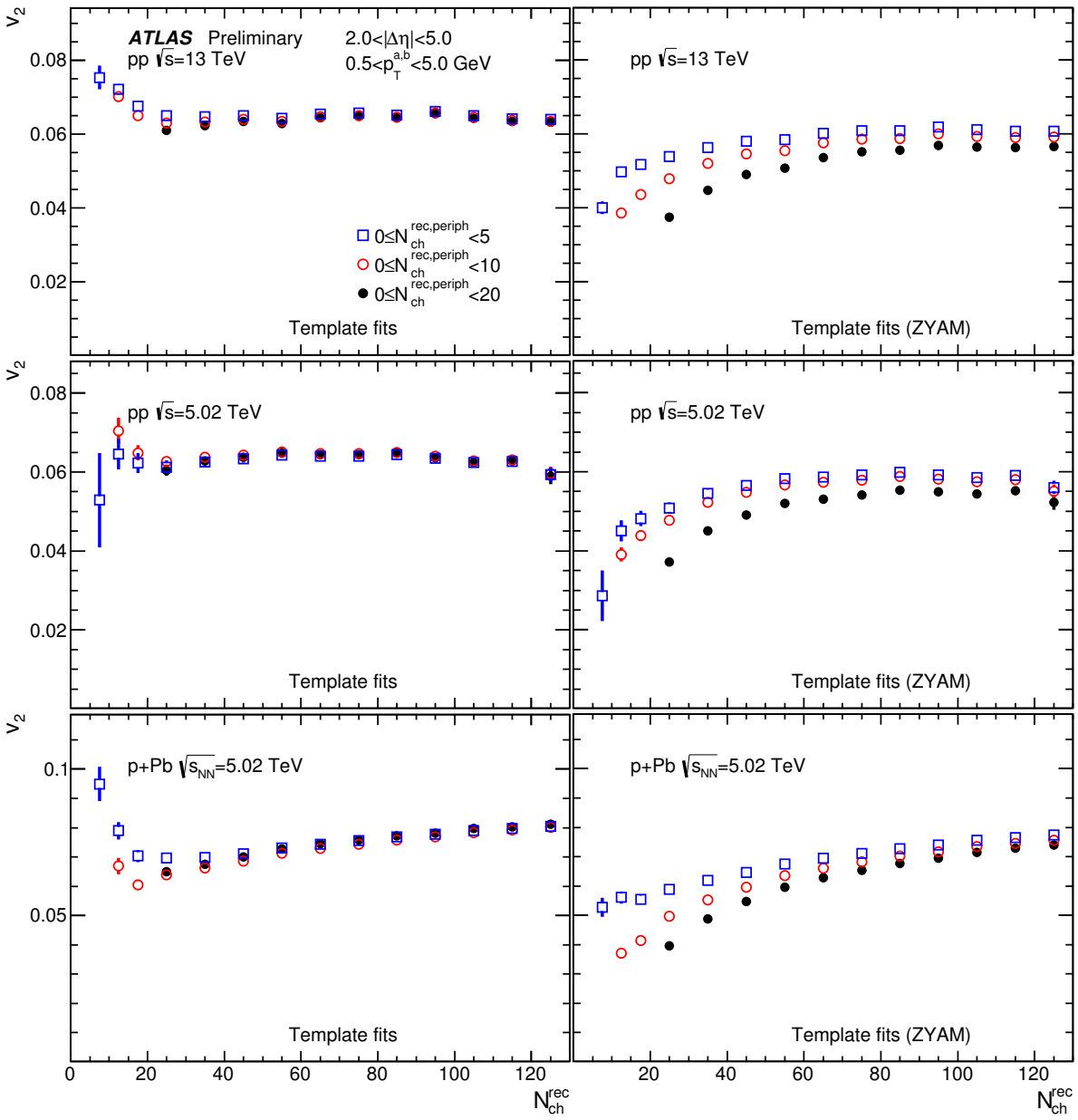

Figure 14: Dependence of the v_2 on the choice of the peripheral bin for the default (left panels) and ZYAM-based (right panels) template fitting methods. The top panels correspond to 13 TeV pp collisions, middle panels correspond to 5.02 TeV pp collisions, and the lower panels correspond to 5.02 TeV p+Pb collisions. The results are plotted as a function of $N_{\mathrm{ch}}^{\mathrm{rec}}$ and for $0.5<p_{\mathrm{T}}^{\mathrm{a,b}}<5.0$ GeV. The error bars indicate statistical uncertainties.

in the 13 TeV pp data varies between 0-3% over the 0–150 $N_{\mathrm{ch}}^{\mathrm{rec}}$ range, and between 0–11% over the 0–150 GeV $E_{\mathrm{T}}^{\mathrm{FCal}}$ range. In the 5.02 TeV data, it varies from 0-4% over the 0–120 $N_{\mathrm{ch}}^{\mathrm{rec}}$ range and 0–11% over the 0-80 GeV $E_{\mathrm{T}}^{\mathrm{FCal}}$ range.

Track reconstruction efficiency: In evaluating the $Y(\Delta\phi)$, each particle is weighted by $1/\epsilon(p_{\mathrm{T}}, \eta)$ to account for the tracking efficiency. The systematic uncertainties in the efficiency, $\epsilon(p_{\mathrm{T}}, \eta)$, thus need to be propagated into the $Y(\Delta\phi)$ and the final $v_{n,n}$ measurements. However, unlike the $Y(\Delta\phi)$, which is strongly affected by the efficiency, the $v_{n,n}$ are mostly insensitive to the tracking efficiency. This is because the $v_{n,n}$ measure the relative variation of the yields in $\Delta\phi$; an overall increase or decrease in the efficiency changes the yields but does not affect the $v_{n,n}$. However, as the tracking efficiency and its uncertainties have p_{T} and η dependence, there is some residual effect on the $v_{n,n}$. The corresponding uncertainty in the $v_{n,n}$ is estimated by repeating the analysis when varying the efficiency to its upper and lower extremes. In the pp analysis, this uncertainty is estimated to be 0.5% for the $v_{2,2}$ and 2.5% for $v_{3,3}$ and $v_{4,4}$. The corresponding uncertainties in the p + Pb data are 0.8%, 1.6% and 2.4% for $v_{2,2}$, $v_{3,3}$ and $v_{4,4}$ respectively.

Pair acceptance: As described in Sec. 4, this analysis uses the mixed-event distributions, $B(\Delta\phi, \Delta\eta)$ and $B(\Delta\phi)$, to estimate and correct for the pair-acceptance of the detector. The mixed-event distributions are in general quite flat in $\Delta\phi$. The Fourier coefficients of the mixed-event distributions, $v_{n,n}^{\mathrm{det}}$, which quantify the magnitude of the corrections, are $\sim 10^{-4}$ in the p+Pb data, and $\sim 2 \times 10^{-5}$ in the pp data. In the p+Pb analysis, potential systematic uncertainties on the $v_{n,n}$ due to residual pair-acceptance effects not corrected by the mixed-events are evaluated following Ref. [13]. This uncertainty is found to be smaller than $\sim 10^{-5}$. In the pp analysis, since the mixed-event corrections are themselves quite small, the entire correction is conservatively taken as the systematic uncertainty.

MC closure: The analysis procedure is validated by measuring the $v_{n,n}$ of reconstructed particles in fully simulated Pythia 8 and HIJING events and comparing them to those obtained using the generated particles. This comparison can test whether the reconstruction introduces unexpected correlations, but it also evaluates the effects of migration in $p_{\mathrm{T}}^{\mathrm{a,b}}$, η, and ϕ which are not accounted for in the measurement. The difference between the generated and reconstructed $v_{n,n}$ is taken to be the MC closure systematic uncertainty. It varies between 10^{-5}–10^{-4} (absolute) in the pp case and between 2–8% (relative) in the p+Pb case, for the different harmonics.

As a cross-check, the dependence of the long-range correlations on the relative charge of the two particles used in the correlation is studied. If the long-range correlations arise from phenomena that correlate only a few particles in an event, such as jets or decays, then a dependence of the correlation on the relative sign of the particles making up the pair is expected. Figure 15 shows the measured v_2 from the template fits for both same and opposite charged pairs. No systematic difference between the two is observed.

Tables 2 and 3 list the systematic uncertainties on the $v_{n,n}$ for the 13 TeV and 5.02 TeV pp data respectively. Most uncertainties are listed as relative uncertainties (in percentages of the $v_{n,n}$), while some are listed as absolute uncertainties. Uncertainties for the p+Pb data are listed in Table 4. The uncertainties associated with tracking efficiency, pair acceptance and MC closure are identical for the 13 and 5.02 TeV data and are listed in Table 2 only. The corresponding uncertainties on the v_n are obtained by propagating the uncertainties on the $v_{n,n}$ when using Eq. (3) to obtain the v_n.

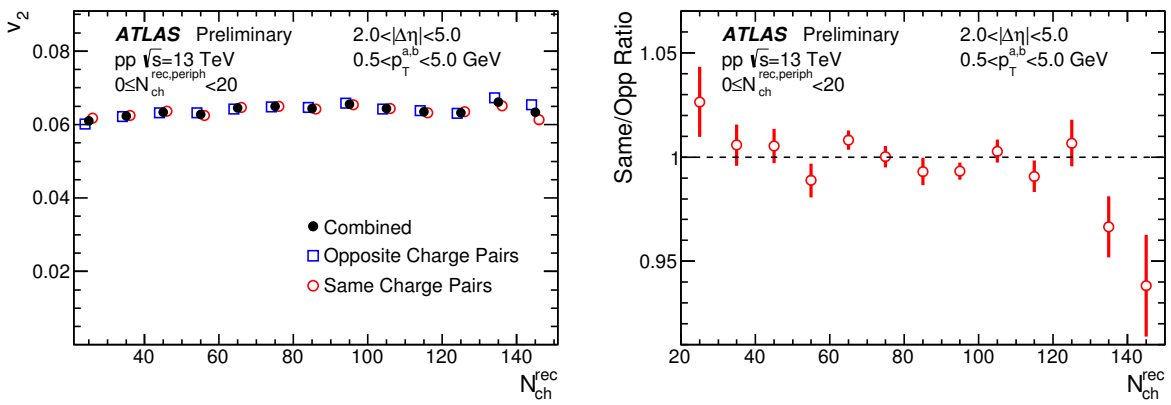

Figure 15: Left Panel : Comparison of the v_2 for same-charge and opposite-charge pairs in the 13 TeV pp data. Also shown are the v_2 values for the two types of pairs combined. Right Panel : ratio of the same-charge to the opposite-charge v_2. The results are for $0.5<p_{\mathrm{T}}^{\mathrm{a,b}}<5$ GeV.

Source	$v_{2,2}$		$v_{3,3}$		$v_{4,4}$	
	$N_{\mathrm{ch}}^{\mathrm{rec}}$ range	syst. unc.	$N_{\mathrm{ch}}^{\mathrm{rec}}$ range	syst. unc.	$N_{\mathrm{ch}}^{\mathrm{rec}}$ range	syst. unc.
Choice of peripheral bin [%]	20–30	7	20–50	>100	20–50	30
$0.5<p_{\mathrm{T}}^{\mathrm{a,b}}<5$ GeV	30–60	7–2	50–100	100–40	50–100	30-10
	>60	2	>100	40	>100	10
Choice of peripheral bin [%]	20–30	6	20–60	40–20		
$1.0<p_{\mathrm{T}}^{\mathrm{a,b}}<5$ GeV	30–60	6–2	60–100	20–10		5
	>80	2	>100	10		
Pileup [%]	0–150	0–3	0–150	0–3	0–150	0–3
Tracking Efficiency [%]		0.5		2.5		2.5
Pair Acceptance (absolute)		2×10^{-5}		2×10^{-5}		2×10^{-5}
MC Closure (absolute)		1×10^{-4}		2×10^{-5}		2×10^{-5}

Table 2: Systematic uncertainties for the $v_{n,n}$ obtained from the template analysis in the 13 TeV pp data. Where ranges are provided for both multiplicity and the uncertainty, the uncertainty varies from the first value to the second value as the multiplicity varies from the lower to upper limits of the range. Where no multiplicity range is provided the uncertainty is multiplicity-independent.

Source	$v_{2,2}$		$v_{3,3}$		$v_{4,4}$	
	$N_{\mathrm{ch}}^{\mathrm{rec}}$ range	syst. unc.	$N_{\mathrm{ch}}^{\mathrm{rec}}$ range	syst. unc.	$N_{\mathrm{ch}}^{\mathrm{rec}}$ range	syst. unc.
Choice of peripheral bin [%]	20–30	8	20–30	55	20–30	>100
$1.0<p_{\mathrm{T}}^{\mathrm{a,b}}<5$ GeV	30–70	8–2	30–50	55–12	>30	50
	>70	2	>50	12		
Pileup [%]	0–120	0–4	0–120	0–4	0–120	0–4

Table 3: Systematic uncertainties for the $v_{n,n}$ obtained from the template analysis in the 5.02 TeV pp data. Where ranges are provided for both multiplicity and the uncertainty, the uncertainty varies from the first value to the second value as the multiplicity varies from the lower to upper limits of the range. Where no multiplicity range is provided the uncertainty is multiplicity-independent. The uncertainties associated with tracking efficiency, pair acceptance and MC closure are identical to those in the 13 TeV pp data (Table 2) and are not listed here.

Source	$v_{2,2}$		$v_{3,3}$		$v_{4,4}$	
	$N_{\mathrm{ch}}^{\mathrm{rec}}$ range	syst. unc.	$N_{\mathrm{ch}}^{\mathrm{rec}}$ range	syst. unc.	$N_{\mathrm{ch}}^{\mathrm{rec}}$ range	syst. unc.
Choice of peripheral bin [%]	20–30	5	20–30	>100	20–30	>100
$0.5<p_{\mathrm{T}}^{\mathrm{a,b}}<5$ GeV	30–250	5–2	30–50	100–40	30–50	100–20
			50–250	40–5	50–250	20–2
Choice of peripheral bin [%]	20–30	12	20–50	55–20	20–50	70–10
$1.0<p_{\mathrm{T}}^{\mathrm{a,b}}<5$ GeV	30–50	12–6	50–100	20–10	50–250	10–5
	50–250	6-2	100–250	10–5		
Pileup [%]	0–300	0-4	0–300	0-4	0–300	0-4
Tracking Efficiency [%]		0.8		1.6		2.4
Pair Acceptance (absolute)		10^{-5}		10^{-5}		10^{-5}
MC Closure [%]		2		4		8

Table 4: Systematic uncertainties for the $v_{n,n}$ obtained from the template analysis in the 5.02 TeV p+Pb data. Where ranges are provided for both multiplicity and the uncertainty, the uncertainty varies from the first value to the second value as the multiplicity varies from the lower to upper limits of the range. Where no multiplicity range is provided the uncertainty is multiplicity-independent.

7 Results

Figure 16 provides a summary of the main results of this note in the inclusive p_{T} interval $0.5<p_{\mathrm{T}}<5$ GeV. It compares the v_n obtained from the the 5.02 TeV, 13 TeV pp and 5.02 TeV p+Pb template fits. The left panels shows v_2, v_3 and v_4 as a function of $N_{\mathrm{ch}}^{\mathrm{rec}}$ while the right panels show the results as a function of $p_{\mathrm{T}}^{\mathrm{a}}$ for the $N_{\mathrm{ch}}^{\mathrm{rec}}\geq 60$ multiplicity range. Due to large statistical and systematic uncertainties in the measured v_3 and v_4 for the 5.02 TeV pp data for $0.5<p_{\mathrm{T}}^{\mathrm{a,b}}<5$ GeV, these data have not been included in the figure but they are shown in Fig. 18 for a different p_{T} interval. Figure 16 shows that the p+Pb v_2 increases with increasing $N_{\mathrm{ch}}^{\mathrm{rec}}$ as previously observed [4] while the pp v_2 is $N_{\mathrm{ch}}^{\mathrm{rec}}$ independent within uncertainties. The p+Pb v_3 is significantly larger than the pp v_3 and also shows a systematic increase with $N_{\mathrm{ch}}^{\mathrm{rec}}$, while the pp v_3 is consistent with being $N_{\mathrm{ch}}^{\mathrm{rec}}$-independent. The pp and p+Pb v_4 are consistent within large uncertainties, and the p+Pb v_4 increases weakly with increasing $N_{\mathrm{ch}}^{\mathrm{rec}}$.

The difference between the pp and p+Pb results for the $N_{\mathrm{ch}}^{\mathrm{rec}}$ dependence of the v_n may not be surprising. Studies of the centrality dependence of the multiplicity distributions in p+Pb collisions show a strong correlation between the multiplicity and the number of participants, or equivalently, the number of scatterings of the proton in the nucleus [72]. Regardless of the interpretation of the results, a dependence of the v_n on the geometry of the p+Pb collisions is unsurprising [73]. In contrast, the relationship between multiplicity and geometry in pp collisions is poorly understood and necessarily different as there are, by definition, only two colliding nucleons. Early studies of this problem accounting for perturbative evolution not only predicted a weak dependence of v_2 on multiplicity but also accurately predicted the two-particle v_2 results obtained in this measurement [74].

The pp and p+Pb $v_2(p_{\mathrm{T}})$ distributions in Fig. 16 show similar trends with both increasing with p_{T} at low p_{T}, reaching a maximum near 3 GeV and decreasing at higher p_{T}. The $v_2(p_{\mathrm{T}})$ distributions for the 5.02 and 13 TeV pp data agree within uncertainties. The p_{T} dependence of the v_3 and v_4 show similar behavior to the v_2 at low p_{T}, where the p+Pb results increase more rapidly with increasing p_{T}. However, unlike the v_2 results, the pp and p+Pb data reach similar values at higher p_{T}. A direct test of the similarity of the p_{T} dependence of the Fourier coefficients in pp and p+Pb collisions is provided in Fig. 17 for $n = 2$. The pp v_2 have been multiplied by 1.51, the ratio (p+Pb to pp) of the maximum v_2 in the top right panel in Fig. 16. The resulting $v_2(p_{\mathrm{T}}^{\mathrm{a}})$ distributions for (scaled) pp and p+Pb agree well for $p_{\mathrm{T}}^{\mathrm{a}}$ up to 5 GeV. At higher $p_{\mathrm{T}}^{\mathrm{a}}$ the pp v_2 decreases more rapidly due to the above-described multiplicity-dependent change in the shape of the dijet peak in the two-particle correlation function at high p_{T}. After the scaling, the pp $v_2(p_{\mathrm{T}}^{\mathrm{a}})$ are slightly higher than the p+Pb at low $p_{\mathrm{T}}^{\mathrm{a}}$, but the similarity in the shapes of the distributions is, nonetheless, striking.

A separate evaluation of the $N_{\mathrm{ch}}^{\mathrm{rec}}$-dependence of the v_2, v_3 and v_4 values is shown in Fig. 18 for the $1<p_{\mathrm{T}}^{\mathrm{a,b}}<5$ GeV interval, where the 5.02 TeV pp measurements yield meaningful v_3 and v_4 results. The figure shows agreement between the 5.02 and 13 TeV pp data for all three Fourier coefficients. It also shows that the p+Pb v_2, v_3 and v_4 rise monotonically with increasing $N_{\mathrm{ch}}^{\mathrm{rec}}$ while the pp results are generally $N_{\mathrm{ch}}^{\mathrm{rec}}$-independent. One possible exception to this statement is that the 13 TeV data indicate a small (~15%) decrease in v_2 in the two lowest $N_{\mathrm{ch}}^{\mathrm{rec}}$ intervals. The pp and p+Pb v_3 and v_4 agree at low $N_{\mathrm{ch}}^{\mathrm{rec}}$ while the v_2 still differs significantly though by a smaller amount than at larger $N_{\mathrm{ch}}^{\mathrm{rec}}$. This behavior is different from that observed in the inclusive p_{T} interval which may, in turn, reflect the convergence of the $v_2(p_{\mathrm{T}})$ distributions between the pp and p+Pb data shown in the top, right panel of Fig. 16.

Measurements [69, 75] and theoretical analyses [76–80] of the correlations between the Fourier coefficients and event plane angles of different flow harmonics in Pb+Pb collisions have indicated significant

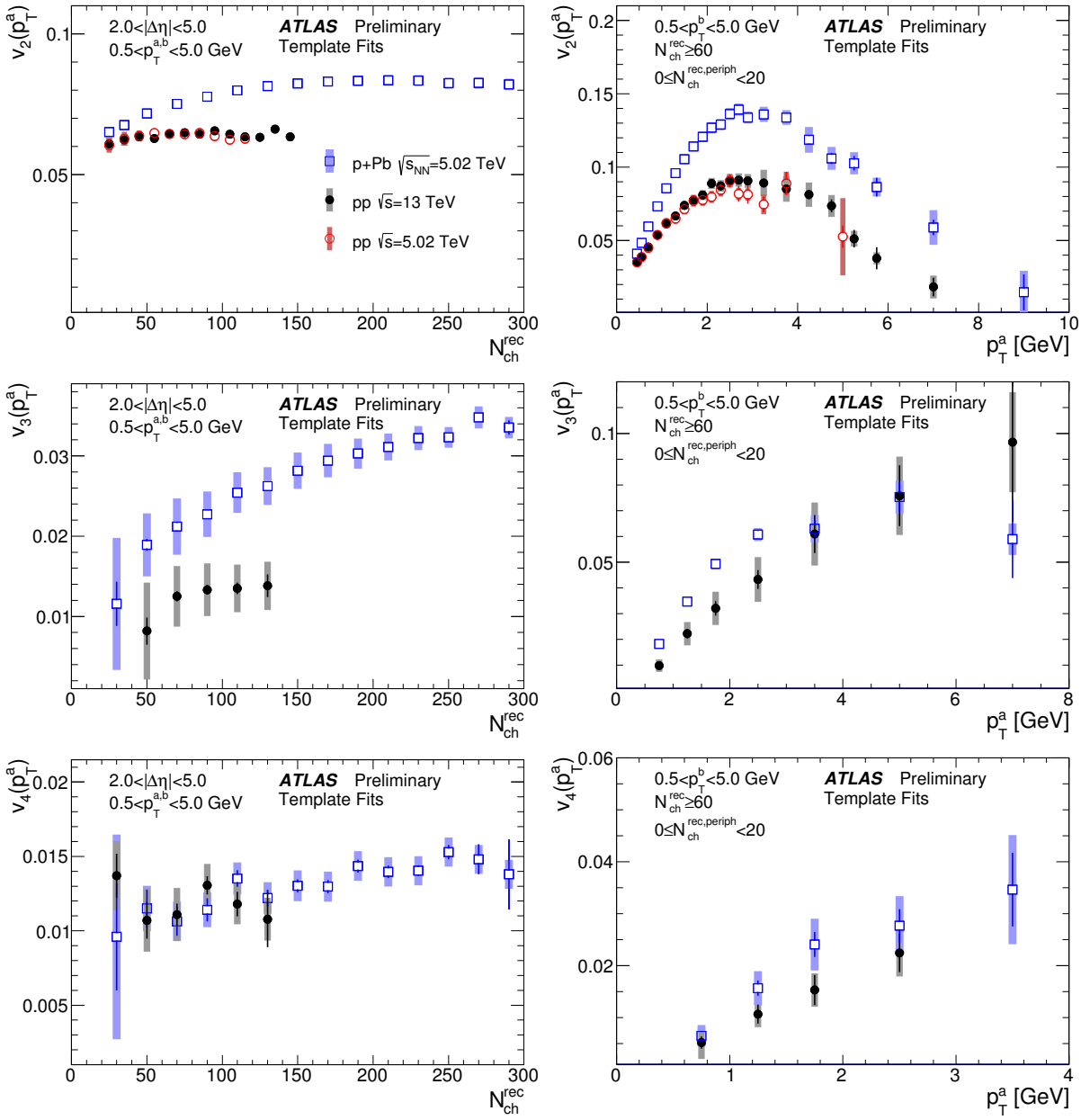

Figure 16: Left Panels: comparison of the v_n obtained from the template fitting procedure in the 13 TeV pp, 5.02 TeV pp, and 5.02 TeV p+Pb data, as a function of $N_{\mathrm{ch}}^{\mathrm{rec}}$. The results are for $0.5<p_{\mathrm{T}}^{\mathrm{a,b}}<5$ GeV. Right Panels: The p_{T} dependence of the v_n for the $N_{\mathrm{ch}}^{\mathrm{rec}}\geq 60$ multiplicity range. From top to bottom the rows correspond to n=2, 3 and 4 respectively. The error bars and shaded bands indicate statistical and systematic uncertainties, respectively.

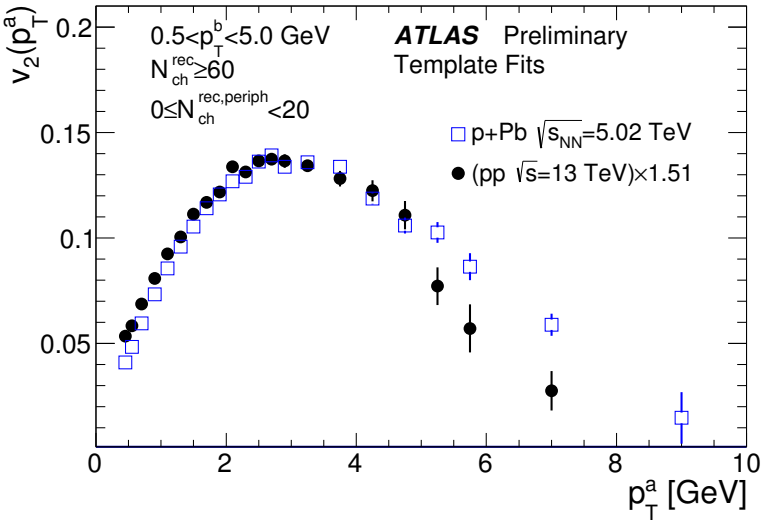

Figure 17: Comparison of the shapes of the $v_2(p_T)$ in the 13 TeV pp and 5.02 TeV p+Pb data. The pp v_2 has been scaled by a factor of 1.51 along the y-axis in order to match the maximum of the v_2 in the two data sets. The results are for 0.5<p_T^b <5 GeVand N_{ch}^{rec} ≥60. The error bars indicate statistical uncertainties.

"non-linearity" resulting from collective expansion such that the response of the medium to an initial elliptic eccentricity can contribute to cos (4ϕ) modulation of the produced particles. In Pb+Pb collisions, the non-linear contribution to v_4 is found to dominate over the geometric contribution except for the most central collisions where the initial-state fluctuations have the greatest impact. The non-linear contribution to v_4 is expect to be proportional to v_2^2 so a comparison of the measured v_4 to v_2^2 in pp and p+Pb collisions may be of interest. The results are presented in Fig. 19, which shows v_4/v_2^2 versus N_{ch}^{rec} for the 13 TeV pp and the p+Pb data. The ratio is observed to be constant as a function of N_{ch}^{rec} for both data sets even though the p+Pb v_2 and v_4 increase with N_{ch}^{rec}. The v_4/v_2^2 ratio is observed to be 50% larger in the pp data than in the p+Pb data. Naively, this would indicate a larger non-linear contribution to the v_4 in pp collisions compared to p+Pb collisions.

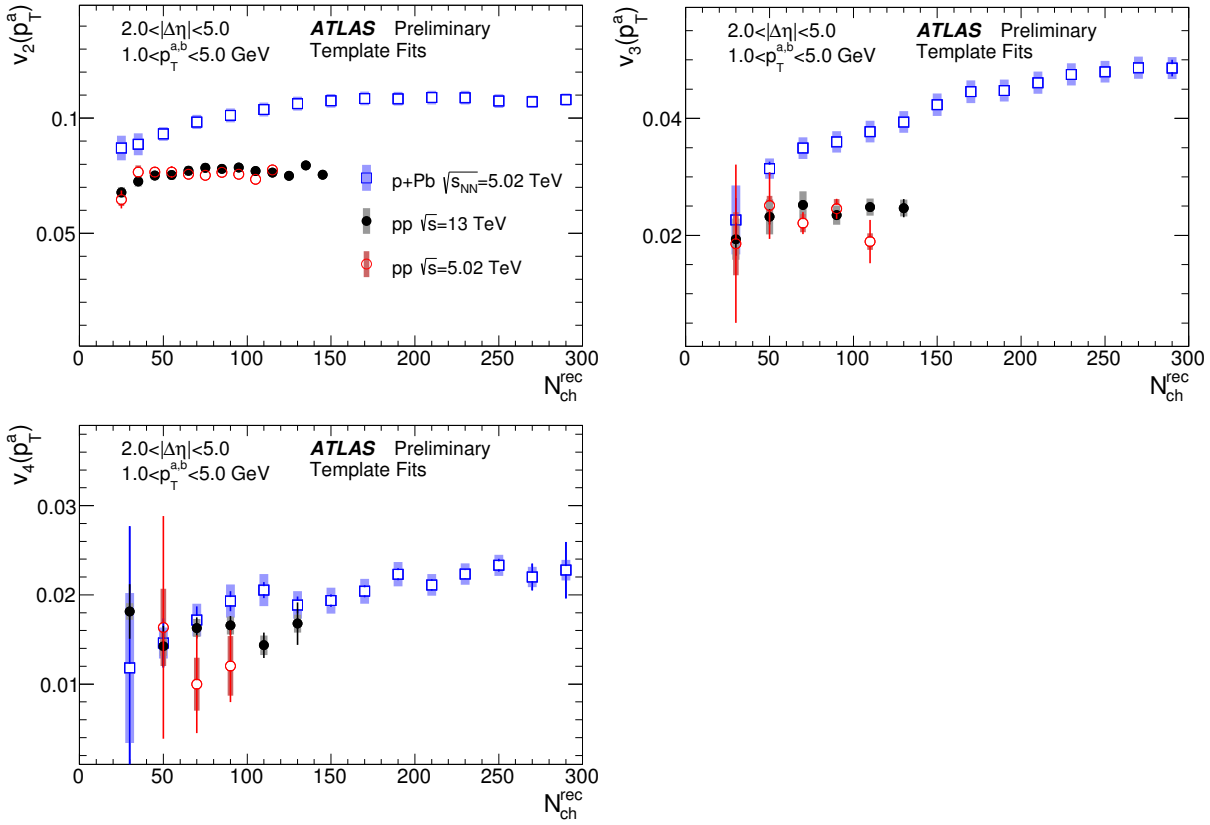

Figure 18: Comparison of the v_n obtained from the template fitting procedure in the 13 TeV pp, 5.02 TeV pp, and 5.02 TeV p+Pb data, as a function of $N_{\mathrm{ch}}^{\mathrm{rec}}$. The results are for $1<p_{\mathrm{T}}^{\mathrm{a,b}}<5$ GeV. The three panels correspond to n=2, 3 and 4. The error bars and shaded bands indicate statistical and systematic uncertainties, respectively.

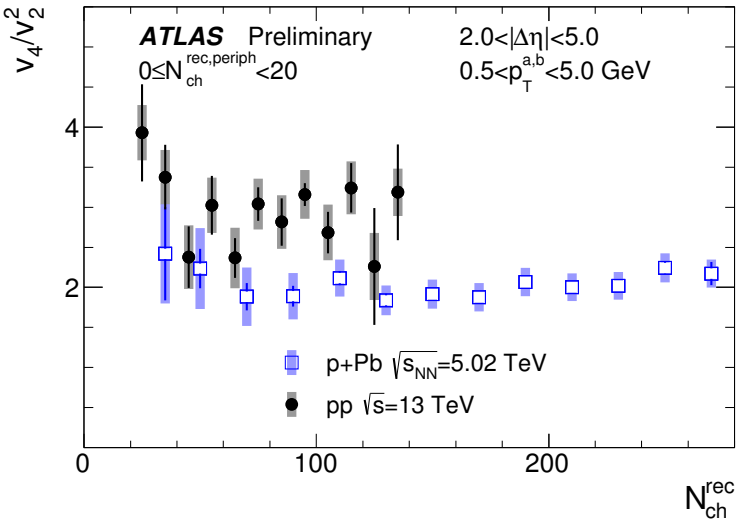

Figure 19: Ratio of the v_4 to the v_2^2 as a function of $N_{\mathrm{ch}}^{\mathrm{rec}}$ in the 13 TeV pp and 5.02 TeV p+Pb data. The results are for $0.5<p_{\mathrm{T}}^{\mathrm{a,b}}<5$ GeV. The error bars and shaded bands indicate statistical and systematic uncertainties, respectively.

8 Conclusion

In summary, this note has presented results of two-charged-particle correlation measurements made by ATLAS in $\sqrt{s}$ = 13 and 5.02 TeV pp collisions and in 5.02 TeV p+Pb collisions at the LHC. The 13 TeV measurements represent an extension of results presented in Ref. [41] using a larger data sample. The p+Pb results are obtained from a re-analysis of Run 1 data presented in Ref. [4] using a template-fitting procedure developed for pp collisions and applied in Ref. [41]. The correlation functions were measured for different intervals of measured charged-particle multiplicity and FCal transverse energy and for different intervals of charged-particle transverse momentum; many of the results were presented for an "inclusive" p_{T} interval $0.5 < p_{\mathrm{T}} < 5$ GeV.

One-dimensional distributions of per-trigger-particle yields as a function of azimuthal angle separation, $Y(\Delta\phi)$, were obtained from the long-range ($|\Delta\eta| > 2$) component of the correlation functions. A template fitting procedure was applied to the $Y(\Delta\phi)$ distributions to remove the contributions from hard-scattering processes and to measure the relative amplitudes, $v_{n,n}$, of the sinusoidal modulation of the soft underlying event. Results for $v_{2,2}$, $v_{3,3}$, and $v_{4,4}$ were obtained for all three colliding systems. An analysis of the factorizeability of the $v_{n,n}$ shows good factorization for most of the measured $N_{\mathrm{ch}}^{\mathrm{rec}}/E_{\mathrm{T}}^{\mathrm{FCal}}$ and p_{T} intervals though factorization was observed to break down for the most extreme combinations of $p_{\mathrm{T}}^{\mathrm{a}}$ and $p_{\mathrm{T}}^{\mathrm{b}}$ in the lowest and highest multiplicity or transverse energy intervals. Since the $v_{n,n}$ results are observed to be consistent with the presence of single-particle modulation of the per-event $\mathrm{d}N/\mathrm{d}\phi$ distributions, single-particle v_n values were extracted and plotted versus $N_{\mathrm{ch}}^{\mathrm{rec}}$ and p_{T}.

Comparisons of the v_2, v_3 and v_4 values between 13 and 5.02 TeV pp collisions show no significant variation in these quantities with center-of-mass energy. As observed in Ref. [41], the v_2 values obtained in pp collisions at both energies are observed to be independent of $N_{\mathrm{ch}}^{\mathrm{rec}}$ within uncertainties for the inclusive p_{T} interval. However, for the $1<p_{\mathrm{T}}<5$ GeV interval a ~15% decrease in v_2 is seen in the lowest $N_{\mathrm{ch}}^{\mathrm{rec}}$ intervals. The p+Pb v_2 values are larger than the pp v_2 values for all multiplicities and are observed to increase slowly with $N_{\mathrm{ch}}^{\mathrm{rec}}$. However, the p+Pb trend appears to converge with the pp values for the lowest multiplicities, at least in the inclusive p_{T} interval. For the $1<p_{\mathrm{T}}<5$ GeV interval, the $v_2(p_{\mathrm{T}})$ trends do not show the same convergence between pp and p+Pb results. Similar to the results for v_2, the pp v_3 and v_4 values are consistent with being independent of $N_{\mathrm{ch}}^{\mathrm{rec}}$ within uncertainties and the p+Pb values are observed to increase with $N_{\mathrm{ch}}^{\mathrm{rec}}$. The pp and p+Pb v_3 and v_4 values are consistent within uncertainties in the lowest measured $N_{\mathrm{ch}}^{\mathrm{rec}}$ intervals.

The p_{T} dependence of the pp and p+Pb v_2 values is similar: both rise approximately linearly with p_{T} and reach a maximum near 3 GeV. The maximum p+Pb v_2 value is approximately 50% larger than the maximum v_2 values for the 13 and 5.02 TeV pp data which are consistent, within uncertainties. The p+Pb v_3 and v_4 values also increase more rapidly with increasing p_{T} than the corresponding pp values for $p_{\mathrm{T}} < 2$ GeV, but the p+Pb v_3 values saturate above 3 GeV while the measured 13 TeV pp v_3 values continue to increase with increasing p_{T} over the full range of the measurement. A test of the similarity of the p_{T} dependence of the pp and p+Pb v_2 values re-scaling pp v_2 values shows that the pp and p+Pb $v_2(p_{\mathrm{T}}^{\mathrm{a}})$ distributions are remarkably similar in shape for $p_{\mathrm{T}}^{\mathrm{a}}<5$ GeV.

An evaluation of the v_4/v_2^2 ratio in the inclusive p_{T} interval shows results that are $N_{\mathrm{ch}}^{\mathrm{rec}}$-independent for both the 13 TeV pp and the p+Pb data. This ratio is observed to be 50% larger for the pp data than for the p+Pb data.

The similarities between the pp and p+Pb results presented here suggest a common physical origin for the azimuthal anisotropies. The difference in the observed multiplicity dependence of the Fourier coefficients likely arises from the different geometry of the pp and p+Pb collisions.

References

[1] ALICE Collaboration, B. Abelev et al., Phys. Lett. **B719** (2013) 29–41, arXiv:1212.2001 [nucl-ex].

[2] ATLAS Collaboration, Phys. Rev. Lett. **110** (2013) 182302, arXiv:1212.5198 [hep-ex].

[3] CMS Collaboration, Phys. Lett. **B724** (2013) 213, arXiv:1305.0609 [nucl-ex].

[4] ATLAS Collaboration, Phys. Rev. C **90** (2014) 044906, arXiv:1409.1792 [hep-ex].

[5] CMS Collaboration, Phys. Rev. Lett. **115** (2015) 012301, arXiv:1502.05382 [nucl-ex].

[6] PHENIX Collaboration, A. Adare et al., Phys. Rev. Lett. **111** (2013) 212301, arXiv:1303.1794 [nucl-ex].

[7] PHENIX Collaboration, A. Adare et al., Phys. Rev. Lett. **114** (2015) 192301, arXiv:1404.7461 [nucl-ex].

[8] STAR Collaboration, L. Adamczyk et al., Phys. Lett. **B747** (2015) 265, arXiv:1502.07652 [nucl-ex].

[9] PHENIX Collaboration, A. Adare et al., Phys. Rev. Lett. **115** (2015) 142301, arXiv:1507.06273 [nucl-ex].

[10] ALICE Collaboration, K. Aamodt et al., Phys. Rev. Lett. **107** (2011) 032301, arXiv:1105.3865 [nucl-ex].

[11] ALICE Collaboration, K. Aamodt et al., Phys. Lett. **B708** (2012) 249–264, arXiv:1109.2501 [nucl-ex].

[12] CMS Collaboration, Eur. Phys. J. **C72** (2012) 2012, arXiv:1201.3158 [nucl-ex].

[13] ATLAS Collaboration, Phys. Rev. C **86** (2012) 014907, arXiv:1203.3087 [hep-ex].

[14] CMS Collaboration, JHEP **1009** (2010) 091, arXiv:1009.4122 [hep-ex].

[15] CMS Collaboration, Phys. Lett. **B718** (2013) 795, arXiv:1210.5482 [nucl-ex].

[16] I. Kozlov et al. (2014), arXiv:1405.3976 [nucl-th].

[17] P. Huovinen et al., Phys. Lett. **B503** (2001) 58, arXiv:hep-ph/0101136.

[18] P. Romatschke and M. Strickland, Phys. Rev. **D68** (2003) 036004, arXiv:hep-ph/0304092.

[19] U. Heinz and R. Snellings, Ann. Rev. Nucl. Part. Sci. **63** (2013) 123, arXiv:1301.2826 [nucl-th].

[20] A. Dumitru et al., Phys. Lett. **B697** (2011) 21, arXiv:1009.5295 [hep-ph].

[21] M. G. Ryskin, A. D. Martin, and V. A. Khoze, J. Phys. **G38** (2011) 085006, arXiv:1105.4987 [hep-ph].

[22] K. Dusling and R. Venugopalan, Phys. Rev. Lett. **108** (2012) 262001, arXiv:1201.2658 [hep-ph].

[23] P. Tribedy and R. Venugopalan, Phys. Lett. **B710** (2012) 125–133, [Erratum: Phys. Lett.B718,1154(2013)], arXiv:1112.2445 [hep-ph].

[24] K. Dusling and R. Venugopalan, Phys. Rev. **D87** (2013) 054014, arXiv:1211.3701 [hep-ph].

[25] K. Dusling and R. Venugopalan, Phys. Rev. **D87** (2013) 094034, arXiv:1302.7018 [hep-ph].

[26] A. Dumitru and V. Skokov, Phys. Rev. **D91** (2015) 074006, arXiv:1411.6630 [hep-ph].

[27] J. Noronha and A. Dumitru, Phys. Rev. **D89** (2014) 094008, arXiv:1401.4467 [hep-ph].

[28] A. Dumitru, A. V. Giannini, and V. Skokov (2015), arXiv:1503.03897 [hep-ph].

[29] T. Lappi, Phys. Lett. **B744** (2015) 315–319, arXiv:1501.05505 [hep-ph].

[30] P. Bozek, Phys. Rev. **C85** (2012) 014911, arXiv:1112.0915 [hep-ph].

[31] P. Bozek and W. Broniowski, Phys. Lett. **B718** (2013) 1557, arXiv:1211.0845 [nucl-th].

[32] A. Bzdak et al., Phys. Rev. **C87** (2013) 064906, arXiv:1304.3403 [nucl-th].

[33] P. Bozek and W. Broniowski, Phys. Rev. **C88** (2013) 014903.

[34] E. Shuryak and I. Zahed, Phys. Rev. **C88** (2013) 044915, arXiv:1301.4470 [hep-ph].

[35] P. Bozek, W. Broniowski, and G. Torrieri, Phys. Rev. Lett. **111** (2013) 172303, arXiv:1307.5060 [nucl-th].

[36] G.-Y. Qin and B. Müller, Phys. Rev. **C89** (2014) 044902, arXiv:1306.3439 [nucl-th].

[37] G. Başar and D. Teaney, Phys. Rev. **C90** (2014) 054903, arXiv:1312.6770 [nucl-th].

[38] M. Habich et al. (2015), arXiv:1512.05354 [nucl-th].

[39] P. M. Chesler, Phys. Rev. Lett. **115** (2015) 241602, arXiv:1506.02209 [hep-th].

[40] P. M. Chesler, JHEP **03** (2016) 146, arXiv:1601.01583 [hep-th].

[41] ATLAS Collaboration, Phys. Rev. Lett. **116** (2016) 172301, arXiv:1509.04776 [hep-ex].

[42] H. Sorge, Phys. Rev. Lett. **78** (1997) 2309, arXiv:nucl-th/9610026.

[43] P. F. Kolb et al., Nucl. Phys. **A696** (2001) 197, arXiv:hep-ph/0103234.

[44] B. Alver and G. Roland, Phys. Rev. **C81** (2010) 054905, [Erratum: Phys. Rev.C82,039903(2010)], arXiv:1003.0194 [nucl-th].

[45] B. Schenke, S. Jeon, and C. Gale, Phys. Rev. Lett. **106** (2011) 042301, arXiv:1009.3244 [hep-ph].

[46] H. Holopainen, H. Niemi, and K. J. Eskola, Phys. Rev. **C83** (2011) 034901, arXiv:1007.0368 [hep-ph].

[47] B. H. Alver et al., Phys. Rev. **C82** (2010) 034913, arXiv:1007.5469 [nucl-th].

[48] H. Petersen et al., Phys. Rev. **C82** (2010) 041901, arXiv:1008.0625 [nucl-th].

[49] G.-Y. Qin et al., Phys. Rev. **C82** (2010) 064903, arXiv:1009.1847 [nucl-th].

[50] F. G. Gardim et al., Phys. Rev. **C85** (2012) 024908, arXiv:1111.6538 [nucl-th].

[51] B. Schenke, P. Tribedy, and R. Venugopalan, Phys. Rev. Lett. **108** (2012) 252301, arXiv:1202.6646 [nucl-th].

[52] F. G. Gardim et al., Phys. Rev. **C87** (2013) 031901, arXiv:1211.0989 [nucl-th].

[53] CMS Collaboration, Phys. Rev. **C92** (2015) 034911, arXiv:1503.01692 [nucl-ex].

[54] ATLAS Collaboration, JINST **3** (2008) S08003.

[55] ATLAS Collaboration, CERN-LHCC-2010-013. ATLAS-TDR-19, URL: http://cds.cern.ch/record/1291633.

[56] ATLAS Collaboration, CERN-LHCC-2012-009. ATLAS-TDR-19-ADD-1, Addendum to CERN-LHCC-2010-013, ATLAS-TDR-019, URL: http://cds.cern.ch/record/1451888.

[57] ATLAS Collaboration, Eur. Phys. J. C **70** (2010) 787, arXiv:1004.5293 [hep-ex].

[58] ATLAS Collaboration, Eur. Phys. J. C **72** (2012) 1849, arXiv:1110.1530 [hep-ex].

[59] ATLAS Collaboration, New J. Phys. **13** (2011) 053033, arXiv:1012.5104 [hep-ex].

[60] A. Salzburger on behalf of the ATLAS Collaboration, J. Phys. Conf. Ser. **664**.7 (2015) 072042.

[61] ATLAS Collaboration, ATL-PHYS-PUB-2015-006, URL: http://cdsweb.cern.ch/record/2002609.

[62] GEANT4 Collaboration, S. Agostinelli et al., Nucl. Instrum. Meth. **A 506** (2003) 250.

[63] ATLAS Collaboration, Eur. Phys. J. C **70** (2010) 823, arXiv:1005.4568 [hep-ex].

[64] X.-N. Wang and M. Gyulassy, Phys. Rev. **D44** (1991) 3501.

[65] T. Sjöstrand, S. Mrenna, and P. Z. Skands, Comput. Phys. Commun. **178** (2008) 852–867, arXiv:0710.3820 [hep-ph].

[66] ATLAS Collaboration, ATL-PHYS-PUB-2011-009, URL: http://cdsweb.cern.ch/record/1363300.

[67] A. Sherstnev and R. S. Thorne, Eur. Phys. J. **C55** (2008) 553, arXiv:0711.2473 [hep-ph].

[68] ATLAS Collaboration, JHEP **1311** (2013) 183, arXiv:1305.2942 [hep-ex].

[69] ATLAS Collaboration, Phys. Rev. C **92** (2015) 034903, arXiv:1504.01289 [hep-ex].

[70] PHENIX Collaboration, A. Adare et al., Phys. Rev. **C78** (2008) 014901, arXiv:0801.4545 [nucl-ex].

[71] N.N. Ajitanand et al., Phys. Rev. C **72** (2005) 011902, arXiv:nucl-ex/0501025.

[72] ATLAS Collaboration, Eur. Phys. J. **C76** (2016) 199, arXiv:1508.00848 [hep-ex].

[73] K. Dusling, W. Li, and B. Schenke, Int. J. Mod. Phys. **E25** (2016) 1630002, arXiv:1509.07939 [nucl-ex].

[74] E. Avsar et al., Phys. Lett. **B702** (2011) 394, arXiv:1009.5643 [hep-ph].

[75] ATLAS Collaboration, Phys. Rev. C **90** (2014) 024905, arXiv:1403.0489 [hep-ex].

[76] Z. Qiu and U. Heinz, Phys. Lett. **B717** (2012) 261, arXiv:1208.1200 [nucl-th].

[77] D. Teaney and L. Yan, Nucl. Phys. **A904-905** (2013) 365c, arXiv:1210.5026 [nucl-th].

[78] D. Teaney and L. Yan, Phys. Rev. **C90** (2014) 024902, arXiv:1312.3689 [nucl-th].

[79] L. Yan and J.-Y. Ollitrault, Phys. Lett. **B744** (2015) 82, arXiv:1502.02502 [nucl-th].

[80] J. Qian, U. W. Heinz, and J. Liu (2016), arXiv:1602.02813 [nucl-th].